

TECHNICAL MEMORANDUM

Declassified by authority of NASA

X-589

Classification Change Notices No. 25Dated ** 12/21/74By Authority of 10/1/63 10/18/71

EXPERIMENTAL INVESTIGATION OF THE PRESSURES, HEAT
TRANSFER, AND SURFACE FLOW PATTERNS AROUND A
BLUNT HALF-CONE LIFTING REENTRY BODY AT
A MACH NUMBER OF 9.6

By Frank S. Coe III and William V. Feller

Langley Research Center
Langley Field, Va.

FACILITY FORM 602

(ACCESSION NUMBER)

N71-75680

(HRL)

(PAGES)

(CODE)

(NASA CR OR TMX OR AD NUMBER)

(CATEGORY)

NATIONAL AERONAUTICS AND SPACE ADMINISTRATION
WASHINGTON

September 1961

NATIONAL AERONAUTICS AND SPACE ADMINISTRATION

TECHNICAL MEMORANDUM X-589

EXPERIMENTAL INVESTIGATION OF THE PRESSURES, HEAT
TRANSFER, AND SURFACE FLOW PATTERNS AROUND A
BLUNT HALF-CONE LIFTING REENTRY BODY AT

A MACH NUMBER OF 9.6*

By Frank S. Coe III and William V. Feller

SUMMARY

Experimental measurements of surface pressure, heat-transfer coefficients, and surface oil-flow patterns are presented for a configuration consisting of a half-cone with a flat canted nose and rounded edges. Tests were made at a Mach number of 9.6 in the Langley 11-inch hypersonic tunnel over an angle-of-attack range from -15° to 45° measured to the flat bottom surface.

The results of the tests show that the bottom surface behaves very much like a blunt-nosed delta wing with cylindrical leading edges, in spite of the short length compared with the blunt-nose width.

The radius of the edge rounding of the nose was chosen to give approximately constant heat-transfer coefficients across the nose flat at the angle of attack for which the nose is normal to the free stream. This objective was fairly well realized, and even for angles of attack up to 10° greater or less than the design angle, the increases in heat-transfer coefficient were moderate. The highest heat-transfer coefficients recorded in the tests occurred at negative angles of attack, for which the stagnation point was on the toroidal corner of the nose.

The surface oil-flow patterns showed extensive regions in which the streak lines were nearly parallel or radial, so that simple local approximations should be adequate for estimating heat transfer. Some regions of more complicated flow were found in which the temperature measurements indicated increased heat-transfer rates.

INTRODUCTION

The advantages to be gained by use of some lift during reentry in reduced decelerations and heating rates, range-control capability, and increased reentry-corridor height over the purely ballistic mode (ref. 1) have led to the study of a variety of shapes characterized by maximum lift-drag ratios on the order of $1/2$. The aerodynamic characteristics of a number of such configurations are summarized in reference 2.

The present investigation was undertaken to study the heat transfer and flow over a shape related to one of these configurations, the L-1. The shape tested was basically a half-cone with a flat canted nose and rounded corners.

The possibility of analytic study of the flow over such a configuration is limited. The body is so short that the blunt-nose flow field can influence the entire afterbody flow, making the validity of simple piecewise approximations like Newtonian and tangent wedge theories somewhat questionable. Therefore, an experimental study of the surface flow patterns and heat transfer was undertaken to help evaluate the feasibility of such a configuration for a reentry vehicle.

SYMBOLS

c_p	specific heat of air at constant pressure
c_w	specific heat of model skin material
D	nose height of model, equals diameter of inscribed disk (see fig. 1)
h	aerodynamic film heat-transfer coefficient, $\left(\frac{q}{T_{aw} - T_w} \right)$
k	thermal conductivity of air
M	Mach number
N_{Pr}	Prandtl number
N_{St}	Stanton number, $\frac{h}{\rho u c_p}$
p	local static pressure

[REDACTED]

τ time
 ϕ coordinate angle for conical surface of model

Subscripts:

D with nose height as characteristic length (see fig. 1)
fp calculated for a flat plate without pressure gradient
l at local static conditions just outside boundary layer
s distance along surface measured from aerodynamic stagnation point in streamwise direction
t at tunnel stagnation conditions
th theoretical value
w refers to model skin
 σ evaluated at conditions just behind a normal shock
 ∞ refers to free-stream conditions

EXPERIMENTAL TECHNIQUE

Tunnel and Test Conditions

The experiments were conducted in the $M = 9.6$ nozzle of the Langley 11-inch hypersonic tunnel, a blowdown facility. A description of the tunnel may be found in reference 3.

The majority of the tests, both heat transfer and pressure, were made at $R_{\infty, D} = 0.118 \times 10^6$. However, some tests were also made at $R_{\infty, D} = 0.095 \times 10^6$ and $R_{\infty, D} = 0.069 \times 10^6$ to check for effects of Reynolds number. The stagnation temperature for all tests was about 1,600° R. In obtaining heat-transfer results, a quick-starting technique was used which approximates the sudden immersion of the model into a fully developed test-section flow. This technique consisted of starting the airflow through the heater and bypassing to atmosphere. When the heater conditions were steady, delivering air at the desired stagnation temperature, the nozzle airflow was started by a quick-opening valve. Heat-transfer data were obtained by measuring transient temperatures at the time at which the stagnation conditions were steady. This time varied between 1.5 and 2.8 seconds. Pressure data were obtained about 60 seconds after the start of flow in order to eliminate the lag in the pressure tubing and cells as a source of error.

Models and instrumentation.- The shape studied, shown in figure 1, is basically half of a 200 half-angle cone. The nose is cut off in a plane making an angle of 55° with the plane of the bottom, and the corners are rounded off to a constant radius in cross section. The true outline of the nose is a segment of an ellipse. It was found, however, that the outline could be closely approximated by a semicircle. For convenience, the curved surface joining the nose flat to the conical surface will be referred to as the toroidal surface.

Two models were used in this investigation; one for heat-transfer and the other for pressure measurements. Both were made from 0.050-inch-thick Inconel sheet. The heat-transfer model was instrumented with a total of 72 chromel-alumel thermocouples formed from 0.010-inch-diameter wire. The wires forming a pair were welded together to form a bead which was inserted into a hole in the surface of the model and welded in place with Inconel. The locations of the temperature-measuring stations are shown in figure 1 and table I. The output of the thermocouples was recorded on 18-channel oscillographs.

Surface pressures were recorded by means of the aneroid-type six-cell recording units described in reference 4. There were 48 pressure orifices (0.060 inch in diameter) located on the model at stations corresponding to certain of the thermocouple locations, as shown in table I.

Data reduction.- Heat-transfer coefficients were determined from the temperature-time records by using the following thin-skin calorimeter equation in which conduction, radiation, and geometric corrections due to curvature of the wall are neglected:

$$\begin{aligned} q &= h(T_{aw} - T_w) \\ &= \rho_w t_w c_w \frac{dT_w}{d\tau} \end{aligned} \quad (1)$$

Inconel properties were obtained from reference 5. For each run, the records were inspected to determine the earliest time at which the air stagnation temperature and pressure could be considered constant. At this time T_w was read, and $\frac{dT_w}{d\tau}$ determined from the slope of the tangent to the temperature-time curve for each thermocouple.

Adiabatic-wall temperature T_{aw} was calculated for each station from the relation

$$\frac{T_{aw}}{T_t} = \frac{1 + \eta_R \frac{\gamma - 1}{2} M_l^2}{1 + \frac{\gamma - 1}{2} M_l^2} \quad (2)$$

Local values of M were calculated from the measured pressure distribution, with the assumption of isentropic expansion from the stagnation-point pressure. For the reduction of the data in this report, the recovery factor was assumed constant at the value

$\eta_R = \sqrt{N_{Pr}} = \sqrt{0.69} = 0.83$. The curve of $\frac{T_{aw}}{T_t}$ with this assumption,

as a function of $\frac{p}{p_t}$, is shown in figure 2. A check was made of the

error involved in this approximation. Values of $\frac{T_{aw}}{T_t}$ calculated with

a varying value of N_{Pr} at T_t' and also for N_{Pr} evaluated at $\frac{T_t + T_l}{2}$ are shown in figure 2. The differences between the curves are small compared with the temperature difference $T_{aw} - T_w$ for the conditions of the present study.

The model at the start of the test airflow is very nearly isothermal, but at the time chosen for data reduction temperature differences have developed because of the varying heat-transfer coefficients. The conduction heat flow in the model skin was estimated for a number of stations on the model, and it was found that over most of the model the conduction heat fluxes were negligible compared to the convection heat-input rates. However, on the curved edges joining the flat nose with the conical and flat surfaces of the afterbody and on the cylindrical edges of the flat bottom, the conduction was not negligible. Unfortunately, these curved regions were so small that it was not practical to install enough instrumentation to permit an accurate conduction calculation. The heat-transfer coefficients are, therefore, presented without correction for conduction. It was estimated that the largest conduction effect was to be found on the toroidal surface at low angles of attack, for which the uncorrected data points might be too low by 30 to 50 percent.

RESULTS AND DISCUSSION

Surface Pressures

The pressure data are presented in the form of ratios of measured surface pressures to p_t' , the total pressure behind a normal shock at the free-stream Mach number. Data from the two rows of orifices nearest the plane of symmetry have been combined and are plotted as though they were on the center line in figures 3(a) and (b), at several angles of attack. The origin of x is arbitrarily fixed at the point of tangency of the nose with the flat bottom.

Newtonian theory predicts, of course, constant pressure on the nose flat and bottom flat, and along the cone element, while the data show considerable variation in all of these regions. In particular, the large pressure changes across the nose flat for angles of attack below 30° and at 45° (and presumably at higher angles also) are significant for heat-transfer estimates (fig. 3(b)). Near $\alpha = 35^\circ$ for which the nose flat is normal to the free-stream direction, the pressures are more nearly constant over the flat portion.

From figure 3(a), it can be seen that over the cone, at 15° angle of attack for which the cone element is inclined only 5° to the free-stream direction the blunt nose induces pressures higher over the entire length of the model than those expected for a sharp cone. For angles of attack of 0° and -10° , however, the nose-induced pressure rise seems to affect only a short region back of the nose. At angles above 30° (fig. 3(b)), where the cone element is in the Newtonian shadow, the pressures change very little with angle of attack or position. Separation cannot, however, be assumed over the entire cone, because of the oil-flow patterns to be discussed subsequently.

On the lower surface, as might be expected from the short chord relative to the nose height, the nose-induced pressures affect the entire bottom, but again as found in the delta-wing tests (ref. 6), the increment of pressure due to the nose becomes relatively smaller as the angle of attack increases, even for distances as short as twice the nose-bluntness height.

Generally, the transverse pressure distribution across the bottom of the model indicated a rise in the pressure toward the edge of the flat bottom (figs. 4(a) and (b)). At angles of attack above 15° , this pressure rise becomes less pronounced with increasing angle of attack. This pattern became more pronounced at the most aft station on the model. This was similar to the behavior of the pressures found on blunt leading-edge delta wings in references 6 and 7.

Because of the similarity of the planform of the model to a blunt delta wing, a direct comparison of the pressures obtained from the present tests was made with those obtained from tests (refs. 6 and 7) of a delta wing having a blunt nose and blunt leading edges. In this comparison, presented in figure 5, the data for both the model of the present investigation and the delta wing represent center-line pressures. Also presented in figure 5 are the pressures predicted by Newtonian theory. Above an angle of attack of 15° , the trend of the results obtained from the present tests was similar to that predicted by Newtonian theory and correlated well with the results obtained for delta wings. Below $\alpha = 15^\circ$, Newtonian theory seriously underestimated



the pressures because of the induced pressures caused by the blunt nose.

Surface Flow Patterns

Two techniques were used for the oil-flow visualization. One was the continuous oil film with added solid particles which formed filaments alined with the oil-flow streamlines. The other was the oil-streamer method, also with solid particles added to the oil, in which oil from a small source was dragged along the surface leaving a wetted trail.

The first method, the oil-film technique, consists of coating the model more or less uniformly with a film of oil containing a suspended solid pigment (lamp black) and then exposing the model to the airflow. As the oil film thins due to the boundary-layer shear, the solid particles tend to form streaks parallel to the oil-flow direction. These streaks become more sharply defined as the oil film gets thinner and tend to remain after the oil film is too thin to flow. The patterns in this condition persist through the tunnel-flow breakdown and can be examined after the run.

L
1
6
0
2

The shear stresses vary considerably over the surface of a model, and the filament pattern develops sooner in the regions of high shear than in regions of low shear. By the time a filament pattern had developed completely in regions of low shear, more often than not the pattern in the region of high shear had disappeared. Because of this disadvantage, the oil-streamer (or oil-dot) method was developed in which oil was applied in small dots all over the model in a reasonably regular pattern with a pen or a small pointed brush. This method gave sharply defined surface streamlines. Some judgment was required in the spacing of the dots in order to obtain adequate detail of the flow pattern without running the streamers together. If the dots are of uniform size the lengths of the streaks give a rough indication of the relative shear stresses. It is necessary to adjust the "stiffness" of the oil-pigment mixture to suit the shear-stress levels of the flow to be studied, but the adjustment is not critical. These dot patterns survive the tunnel-flow breakdown very well and are usually recorded by photographing the model outside the tunnel. Results obtained in the present investigation by the dot technique are shown in figure 6. Because of the high shear stresses over most of the model, the dot technique was used for all angles of attack. However, the oil-film technique was tried at $\alpha = 35^\circ$ with good results over the aft portion of the model (fig. 6(h)).

Examination of the flow patterns obtained revealed some very interesting phenomena.



On the nose, as the angle of attack increases from -20° , the stagnation point moves from a point on the toroidal surface to the nose flat at about 30° to 40° , and then onto the cylindrical transition surface. At very low angles of attack, -20° to 0° , the oil-flow lines over the nose flat are nearly straight and parallel. At large angles of attack, 50° and 60° , the flow lines become nearly radial over the nose flat.

On the conical part of the model at negative angles of attack (figs. 6(a) and (b)), the oil-flow patterns show a dividing streamline on the most windward cone element, $\phi = 90^\circ$. At $\alpha = 0^\circ$ (fig. 6(c)), the flow lines are about parallel to the cone elements except near the flat bottom where there is a bleed off of air from the cone into the lower pressure region of the flat bottom. For $\alpha = 10^\circ$ (fig. 6(d)), the oil-flow pattern indicated the existence of parallel flow. At an angle of attack of 35° the oil-dot technique (fig. 6(g)) indicated low shear over much of the cone, suggesting separated flow. However, the oil-film technique at this angle (fig. 6(h)) did not show separation but indicated a rather unusual flow pattern which was caused by the bleed off of air from the high-pressure region of the bottom into the low-pressure region of the conical afterbody. It was felt, however, that above $\alpha = 40^\circ$ separation did occur.

On the flat bottom, the pattern of the oil streaks streaming back from the nose hinted at the existence of a pair of vortices originating from the two corners. This pattern was observed to occur at angles of attack of -20° and -10° (figs. 6(a) and (b)). At $\alpha = 10^\circ$ the stagnation line moved from the cone to the cylindrical surface between the cone and the bottom. The stagnation line remained on the cylindrical surface through $\alpha = 35^\circ$. Above $\alpha = 35^\circ$ the flow lines indicate the same type of dividing stream line that was demonstrated on delta wings in reference 6. The flow pattern at $\alpha = 35^\circ$ and 40° was linear and parallel over much of the span.

At $\alpha = 35^\circ$, when the nose flat is normal to the free stream, a calculation of the inviscid flow stream lines was made, results of which are shown in figure 7. The method of calculation was the same as that developed at the 11-inch hypersonic tunnel for a delta wing at $\alpha = 90^\circ$ presented in references 6 and 8.

A circular disk with rounded edges was inscribed in the nose, matching the cross section of the nose in the plane of symmetry of the model. The nose of the actual model was considered a semicircle in outline. It was then assumed that the velocity components normal to the semicircular part of the periphery and to the straight edge of the actual model were independent of each other and had the same dependence on distance from the boundary as was found for the inscribed circular

disk. With these assumptions a family of radial velocity vectors was constructed to represent the effect of the circular edge, and a family of parallel vectors was constructed to represent the effect due to the straight edge. Typical values are shown in the left-hand side of figure 7. The magnitude of the vectors of each family decreases to zero at a distance from the corresponding edge equal to the radius of the inscribed disk. In the regions where components due to both edges occur, the components are added. From the vector field so constructed, the streamlines are drawn with the vectors as tangents.

In the lower part of figure 7 the calculated streamlines are compared with the oil-flow pattern over the nose. The general qualitative agreement is good, verifying the approximation in the construction that there are regions of flow influenced by only one of the edges, giving radial streamlines near the circular arc edge and parallel streamlines near the straight edge.

L
1
6
0
2

Schlieren Photographs

Schlieren photographs of the flow over the model are shown in figure 8 for several angles of attack. At $\alpha = -10^\circ$ and 0° , the shock standoff distance and curvature are determined by the small radius of the toroidal surface. At high angles of attack of 30° and above, the nose height determines the shock shape. It is interesting to note that the position and shape of the forward portion and upper limb of the shock with respect to the undisturbed free stream change very little with angle of attack of the model between 30° and 40° .

Heat-Transfer Results

The results of the heat-transfer tests are presented without correction for heat conduction in the model for reasons previously mentioned.

In designing the nose of the model, the ratio of edge radius to equivalent nose disk radius was chosen as 0.5 to give an approximately constant heat-input rate over the nose flat at an angle of attack of 35° where the nose is normal to the airstream. The results of the tests showed that this objective was fairly well realized, and the heat transfer was fairly constant over the nose flat for angles of attack of 30° , 35° , and 40° (figs. 9(b) and (c)). The highest heat-transfer coefficient in any of the tests was noted to be on the torus at $\alpha = -15^\circ$ (fig. 9(a)).

The heat transfer over much of the conical afterbody at an angle of attack of 0° (fig. 10(a)) was fairly constant with the exception of the region near the toroidal surface. For angles of attack of 25° to 45° (figs. 10(a) and (b)) the heat transfer over much of the conical

afterbody was low with the exception of the region defined by $\phi = 20^\circ$ and 160° . Heat transfer for $\phi = 20^\circ$ and 160° changed less throughout the entire angle-of-attack range tested than other values of ϕ . It should be stated here that for figures 9 to 14 the fairings are intended only to connect points.

It may be seen that the circumferential heat-transfer distributions (fig. 11) were similar at successive stations back on the body, with the exception of the behavior of the heat transfer at the most aft station, station 2.75, at angles of attack of 40° and 45° . It is of interest to note that with the exception of $\alpha = -15^\circ$ the heat transfer was highest on the cylindrical surface between the conical afterbody and the flat bottom. This was similar to the results obtained for the delta wing (ref. 6).

The oil-flow patterns on the flat bottom of the model for negative angles of attack showed disturbances that suggest vortices streaming off each corner of the nose. In the heat-transfer measurements at $\alpha = -15^\circ$ at the rearmost station, figure 11(d), there is a high heat-transfer coefficient recorded by the thermocouple at $y = 0.62$ inch from the center line, which is within the area showing increased shear in the oil flow. At more forward locations (figs. 11(a), (b), and (c)), no clear indication of locally increased heating can be seen, but the thermocouple spacing is too large to prove that some increase does not occur in the area indicated by the oil-flow patterns.

A check was made to find out the possible effect of Reynolds number on heat transfer (figs. 12 and 13). For an angle of attack of 15° (fig. 12) the data from stations 1.25 and 2.00 at several stream unit Reynolds numbers fall along a single curve. However, at the rearmost station (station 2.75) on the conical afterbody, the several stream Reynolds numbers gave considerably different curves. At $\alpha = 15^\circ$ the conical afterbody sees the flow in the sense of Newtonian theory.

This effect of Reynolds number on the conical afterbody at $\alpha = 30^\circ$ in figure 13 is much smaller. It is possible that the behavior of the heat transfer at $\alpha = 15^\circ$ indicates the presence of some transitional boundary-layer flow at the rear station on the cone.

Figure 14(a) shows the heat-transfer parameter near the center line of the flat bottom of the model plotted against angle of attack. The curves at angles of attack above 20° show the same trend with α as does $\sqrt{\frac{p}{p_t}}$ which is also shown. Therefore, local flat-plate theory should be adequate for predicting the heat transfer for angles of attack above 20° .

On the cylindrical surface between the conical afterbody and the flat bottom, the highest heat transfer occurs at the station nearest the nose at $\alpha = 0^\circ$ (fig. 14(b)). With increasing angle of attack the heat transfer becomes more nearly independent of distance from the nose. The distance from the nose is seen to have a large effect on the heat transfer on the cylindrical surface at low angles of attack (-15° to 15°). However, above $\alpha = 15^\circ$ the heat transfer is little affected by the presence of the nose. This result is analogous to previous results obtained from delta-wing tests (ref. 6).

On the center line of the conical afterbody (fig. 14(c)) the trend with angle of attack was as expected with the exception of the behavior of location 37 at the most aft station (2.75). There unfortunately was insufficient instrumentation to explore those unusual results further.

In figure 14(d) the behavior of a fixed point (locations 1 and 4) as the stagnation point moves is illustrated. Locations 13, 16, and 14 show far less effect of α on heat transfer.

Comparison With Theory and Delta-Wing Data for Flat Bottom

In figure 15 the heat-transfer results obtained for the flat bottom (along the center line) were compared with data obtained from previous tests of delta wings having blunt noses and blunt leading edges and with local flat-plate theory.

The reference value $h_{t,th}$ was calculated for the center of a flat-nose disk with rounded edges that could be inscribed in the nose of the model tested. The relation for stagnation-point heating on a body of revolution (ref. 9) was used:

$$\frac{hD}{k_\sigma} = 0.736 N_{Pr}^{0.4} \left(\frac{D}{u_\sigma} \frac{du}{dx} \right)_{x=0}^{1/2} \left(\frac{\rho_\sigma u_\sigma D}{\mu_\sigma} \right)^{1/2} \quad (3)$$

where the subscript σ denotes values for conditions just behind a normal shock and $\left(\frac{D}{u_\sigma} \frac{du}{dx} \right)_{x=0}$ was evaluated from the correlation of rounded-disk data presented in reference 6, for a ratio of edge to disk radius $\frac{r}{D/2} = 0.51$. The conditions assumed for the calculation were:

$$M_\infty = 9.65$$

$$p_t = 45 \text{ atm}$$

$$T_t = 1,610^\circ \text{ R}$$

$$D = 1.10 \text{ in.}$$

$$\left(\frac{D}{u_\sigma} \frac{du}{dx} \right)_{x=0} = 4.14$$

All values of h obtained from both the theory and the tests were divided by this reference value.

The local flat-plate theory used in calculating the theoretical heat-transfer coefficients was based on that given in reference 10. The coefficients for a blunt-nose flat plate with zero pressure gradient were first calculated by using the T-prime method and the modified Reynolds analogy applied to the Blasius skin-friction value:

$$N_{St,fp} \sqrt{R_{fp,s}} = \frac{0.332}{\sigma_{fp}} \sqrt{C'} \quad (4)$$

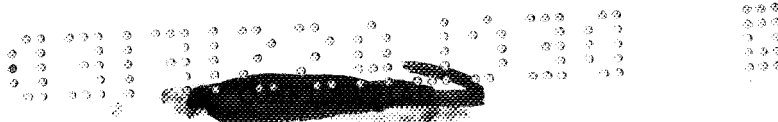
where

$$C' = \frac{\mu_{fp}' T_{fp}}{\mu_{fp} T_{fp}'}$$

The Reynolds analogy factor $\sigma_{fp} = N_{Pr}^{2/3}$ was evaluated at T_{fp}' . (Values of N_{Pr} for air are tabulated in ref. 11.) The subscript fp denotes the reference conditions existing on a blunt-nose flat plate at zero angle of attack, with a pressure equal to free-stream static pressure. The Monaghan T-prime equation as given in reference 10 was used:

$$\frac{T_\infty'}{T_\infty} = \frac{T_w}{T_\infty} + 0.468 N_{Pr}^{1/3} \left(\frac{T_r}{T_\infty} - \frac{T_w}{T_\infty} \right) - 0.273 N_{Pr} \frac{\gamma - 1}{2} M_\infty^2 \quad (5)$$

Substituting $N_{Pr} = 0.685$, rearranging, and rewriting in the notation used in this text reduces equation (5) to



$$\frac{T_{fp}'}{T_{fp}} = 0.4125 + 0.5875 \frac{T_w}{T_{fp}} + 0.0302 M_{fp}^2 \quad (6)$$

The resulting value of h_{fp} obtained was then corrected for effects of pressure by

$$\frac{h}{h_{fp}} = K_3 \left(\frac{p}{p_{fp}} \right)^{1/2} \quad (7)$$

where $p_{fp} = p_\infty$ and K_3 was assumed equal to 1.

The results from the above calculations are presented in figures 15(a) and (b) along with actual measured values of h from the test on the model and from a blunt-nose delta wing. As can be seen at the higher angles of attack the local flat-plate theory is a fairly good first approximation to the center-line distribution of heat transfer. The data obtained from the tests also compare favorably with data from previous delta-wing tests at all angles of attack.

CONCLUDING REMARKS

Experimental measurements of surface pressure, heat-transfer coefficients, and surface oil-flow patterns were presented for a configuration consisting of a half-cone with a flat canted nose and rounded edges.

The flat bottom, despite the wide blunt nose and short chord, was found to behave very much like the sphere-nose delta wing. The effect of the nose on pressures decreased with angle of attack, and could be reasonably neglected for angles of attack above 15° for distances as short as twice the nose height from the nose. At lower angles of attack, zero and below, the heat transfer was less than would be predicted from the measured pressures as was the case for the delta wing but showed also local regions of increased shear and heat transfer due possibly to vortices originating at the corners of the nose.

The nose is approximately semicircular in outline, but it was found that the pressure distribution of the inscribed circular disk furnished a basis for constructing the streamlines and estimating the stagnation-point heat-transfer rates for the angle of attack where the nose is normal to the stream ($\alpha = 35^\circ$).

L
1
6
0
2



REFERENCES

1. Lees, Lester, Hartwig, Frederic W., and Cohen, Clarence B.: Use of Aerodynamic Lift During Entry Into the Earth's Atmosphere. ARS Journal, vol. 29, no. 9, Sept. 1959, pp. 633-641.
2. Rainey, Robert W., Compiler: Summary of Aerodynamic Characteristics of Low-Lift-Drag-Ratio Reentry Vehicles From Subsonic to Hypersonic Speeds. NASA TM X-588, 1961.
3. Bertram, Mitchel H.: Boundary-Layer Displacement Effects in Air at Mach Numbers of 6.8 and 9.6. NASA TR R-22, 1959. (Supersedes NACA TN 4133.)
4. McLellan, Charles H., Williams, Thomas W., and Bertram, Mitchel H.: Investigation of a Two-Step Nozzle in the Langley 11-Inch Hypersonic Tunnel. NACA TN 2171, 1950.
5. O'Sullivan, William J., Jr.: Some Thermal and Mechanical Properties of Inconel at High Temperatures for Use in Aerodynamic Heating Research. Proc. A.S.T.M., vol. 55, 1955, pp. 757-763.
6. Bertram, Mitchel H., Feller, William V., and Dunavant, James C.: Flow Fields, Pressure Distributions, and Heat Transfer for Delta Wings at Hypersonic Speeds. NASA TM X-316, 1960.
7. Bertram, Mitchel H., and Henderson, Arthur: Recent Hypersonic Studies of Wings and Bodies. [Preprint] 1131-60, Am. Rocket Soc., May 1960.
8. Phillips, William H.: Research on Blunt-Faced Entry Configurations at Angles of Attack Between 60° and 90° . NASA TM X-315, 1960.
9. Crawford, Davis H., and McCauley, William D.: Investigation of the Laminar Aerodynamic Heat-Transfer Characteristics of a Hemisphere-Cylinder in the Langley 11-Inch Hypersonic Tunnel at a Mach Number of 6.8. NACA Rep. 1323, 1957. (Supersedes NACA TN 3706.)
10. Bertram, Mitchel H., and Feller, William V.: A Simple Method for Determining Heat Transfer, Skin Friction, Boundary-Layer Thickness for Hypersonic Laminar Boundary-Layer Flows in a Pressure Gradient. NASA MEMO 5-24-59L, 1959.
11. Hilsenrath, Joseph, Beckett, Charles W., et al: Tables of Thermal Properties of Gases. NBS Cir. 564, U.S. Dept. Commerce, 1955.

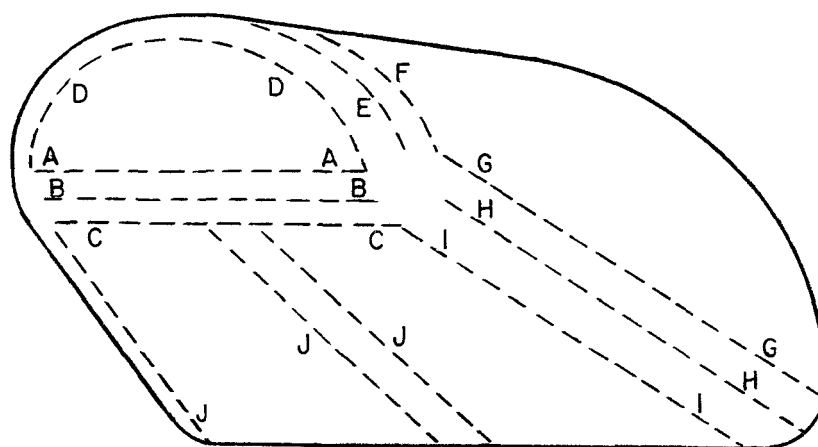
TABLE I.- PRESSURE-ORIFICE AND THERMOCOUPLE LOCATIONS ON MODEL

Location	Instru- mentation (a)	Y, in.	z, in.	ϕ , deg	θ , deg	Station	Note (b)	Location	Instru- mentation (a)	Y, in.	z, in.	ϕ , deg	θ , deg	Station	Note (b)
1	T and P	-0.125	0.450			---		37	T and P			100		2.75	E
2	T and P	+.250	.450			---		38	T			120			D
3	T and P	-.375	.300			---		39	T and P			140			F
4	T	+.125	.300			---		40	T and P			140		.75	
5	T and P	-.125	.200			---		41	T			140		1.25	
6	T	+.250	.200			---		42	T and P			140		2.00	
7	T and P	-.375	----			---	A	43	T			140		2.75	
8	T and P	+.125	----			---	A	44	T and P			140			E
9	T and P	+.500	----			---	A	45	T and P			140		.50	
10	T	-.500	----			---	B	46	T and P			160		1.00	
11	T and P	-.125	----			---	B	47	T			160			
12	T and P	+.375	----			0.75	G	48	T and P				7		B at H
13	T					2.75	G	49	T and P						C at I
14	T					.50	G	50	T and P						C
15	T and P					1.00	G	51	T and P				14		C at J
16	T and P					2.50	G	52	T and P						C
17	T and P						D	53	T and P					.875	C at H
18	T and P			20			F	54	T						H
19	T and P			20		.75		55	T				14		
20	T and P			20		1.25		56	T				7		I
21	T and P			20		2.00		57	T					.875	I
22	T and P			20		2.75		58	T and P					1.25	
23	T and P			20			E	59	T				7	1.25	J
24	T			40			D	60	T and P				14	1.25	
25	T and P			60			F	61	T and P					1.25	H
26	T and P			60		.75		62	T				14	2.00	H
27	T			60		1.25		63	T and P					2.00	J
28	T			60		2.00		64	T and P				7	2.00	I
29	T and P			60		2.75		65	T					2.00	H
30	T and P			60			E	66	T and P				14	2.75	J
31	T and P			80		.75		67	T and P				7	2.75	I
32	T			80		2.00		68	T				14	2.75	H
33	T			100			D	69	T and P				7	2.75	J
34	T and P			100		1.25	F	70	T and P					2.75	I
35	T and P			100				71	T and P					2.75	
36	T and P			100				72	T					2.75	

^aThe letter T stands for thermocouple, and the letter P stands for pressure orifice.

^bSee next page for explanation of letter notation.

TABLE I.- PRESSURE-ORIFICE AND THERMOCOUPLE
LOCATIONS ON MODEL - Concluded



Explanatory Notes

- A Line of tangency between flat nose and cylinder connecting nose to flat bottom
- B 28° from line of tangency between flat bottom and cylinder connecting nose to bottom (midway between lines A and C)
- C Line of tangency between flat bottom and cylinder connecting nose to flat bottom
- D Line of tangency between flat nose and toroidal surface
- E 53° from line of tangency between flat nose and toroidal surface (midway between lines D and F)
- F Line of tangency between toroidal surface and conical afterbody
- G Line of tangency between conical afterbody and cylindrical surface connecting the conical afterbody with the flat bottom
- H 45° from line of tangency between flat bottom and cylindrical surface connecting the bottom with the conical afterbody
- I Line of tangency between flat bottom and cylindrical surface connecting the bottom with the conical afterbody
- J $\theta = 0^\circ$ (0.125 inch from center line of bottom surface)

L
1
6
0
2

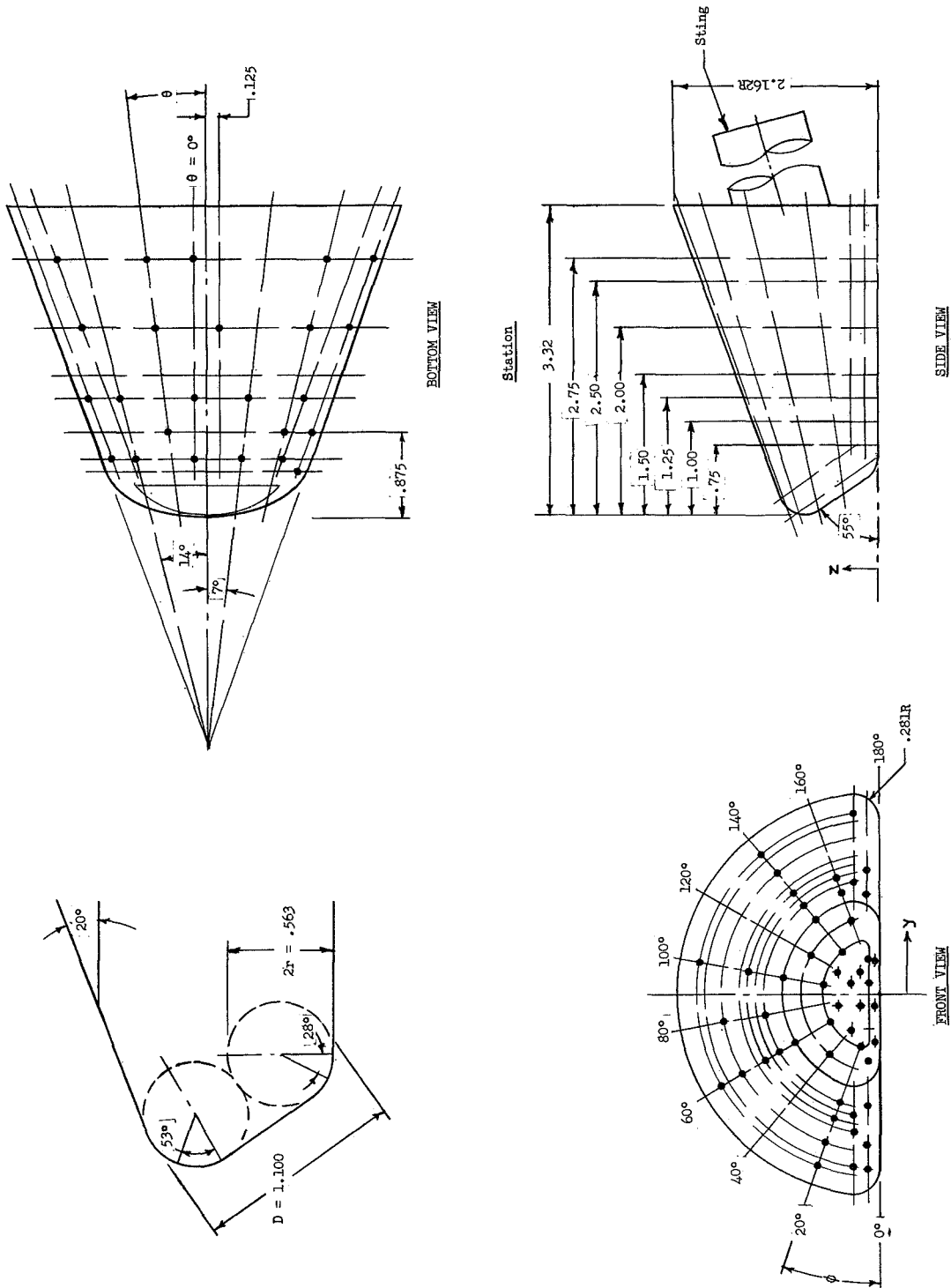


Figure 1.- Model and instrumentation layout. (All dimensions are in inches.)

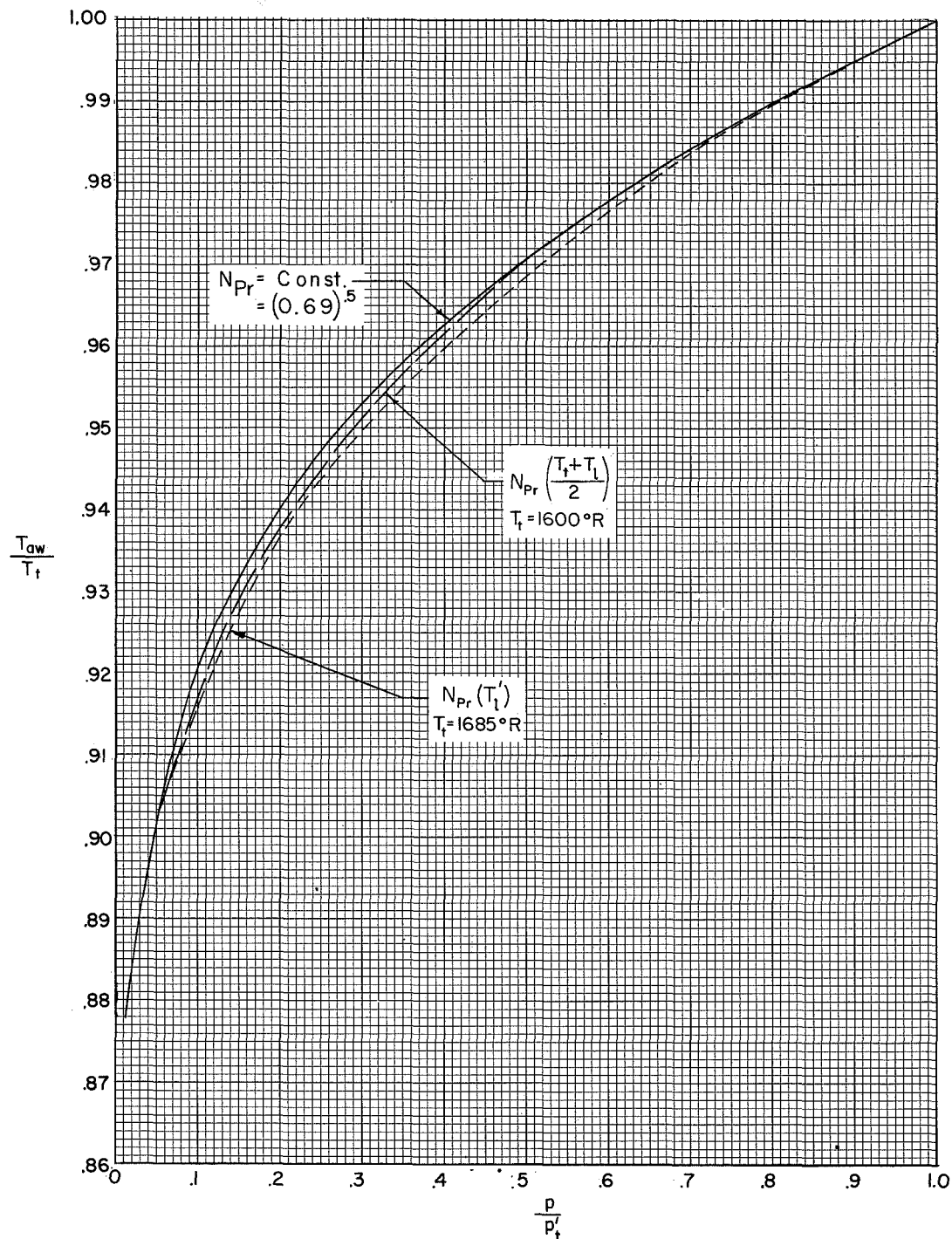
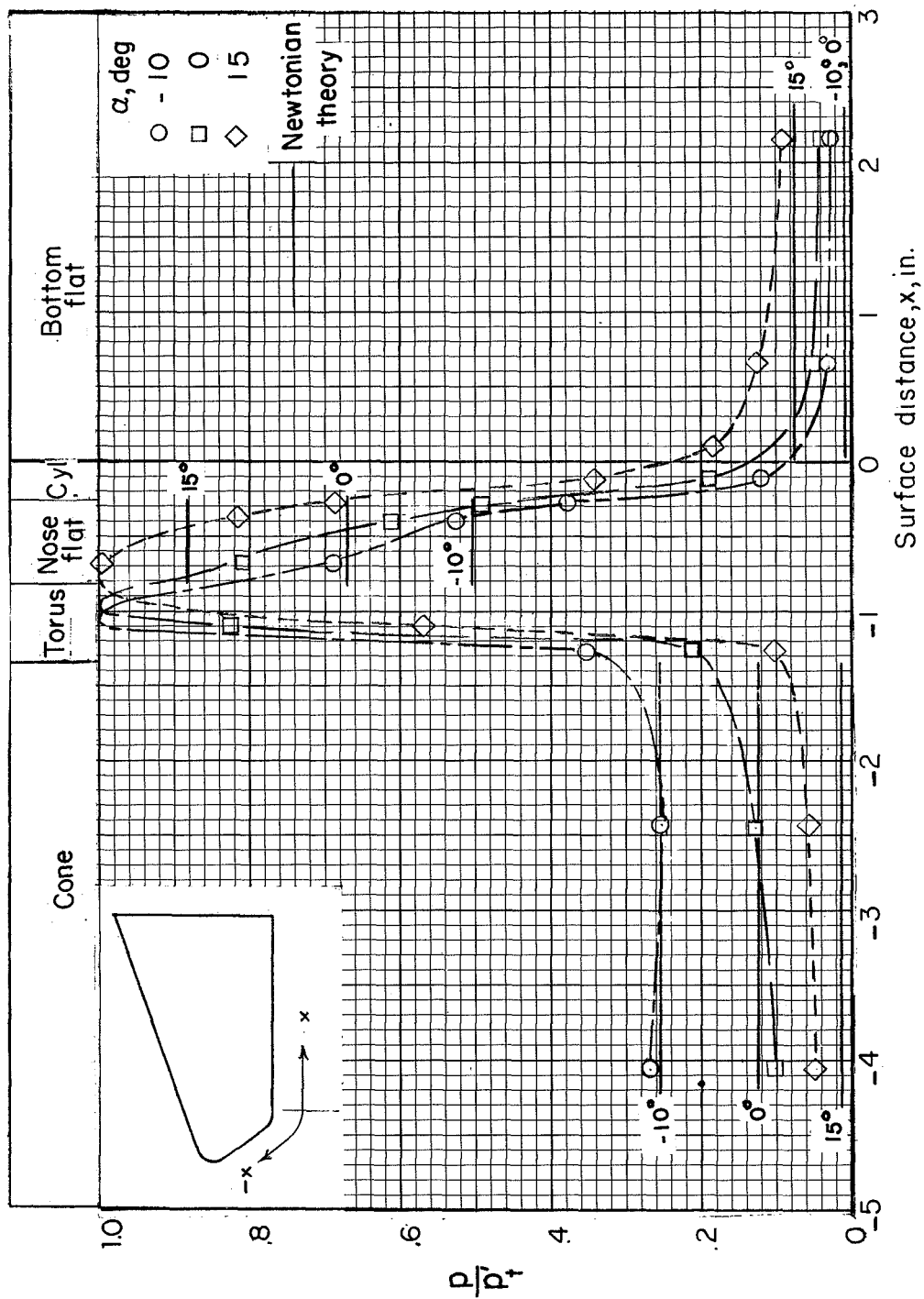
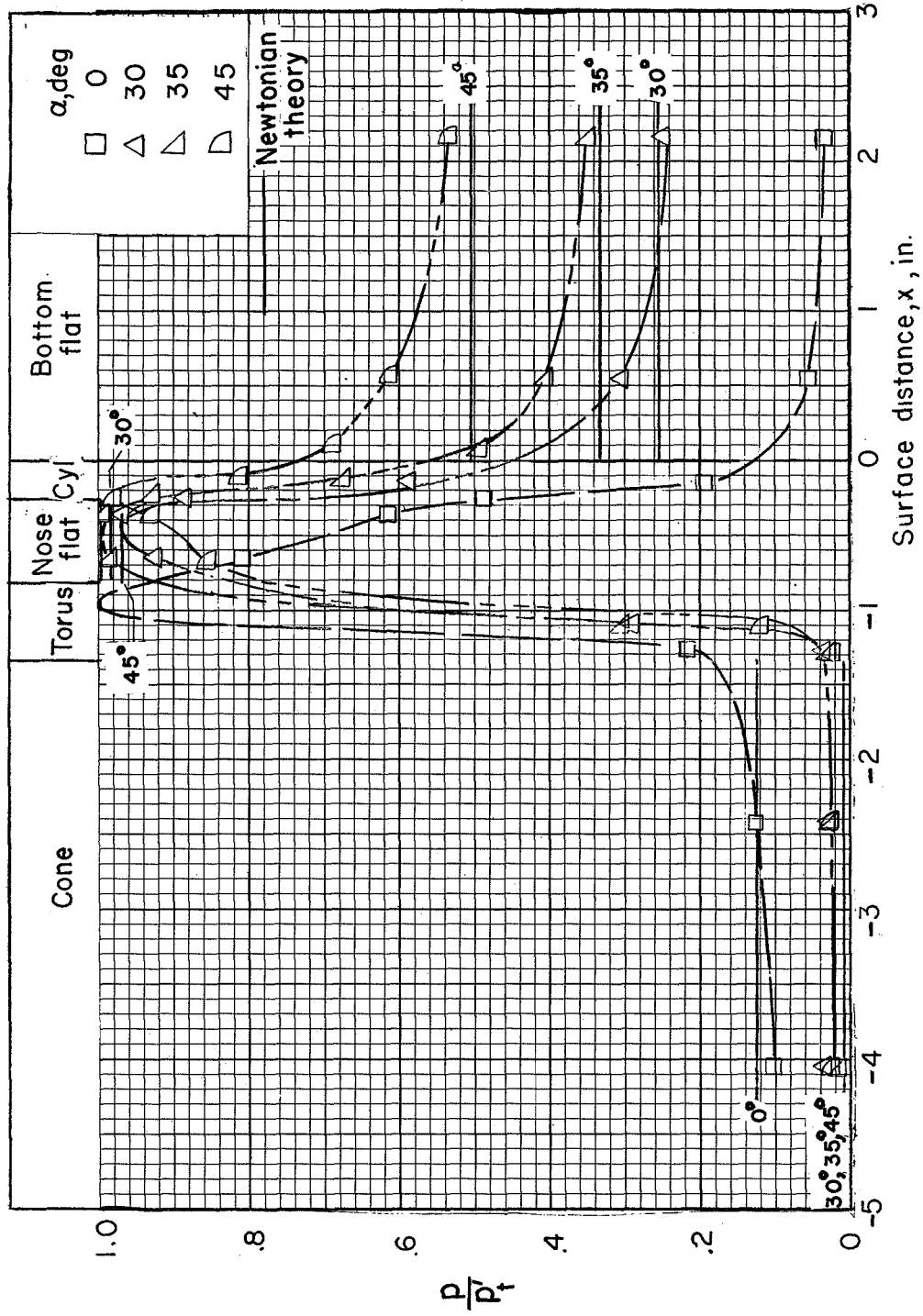


Figure 2.- Relation between recovery temperature and local pressure for isentropic flow from the stagnation point.



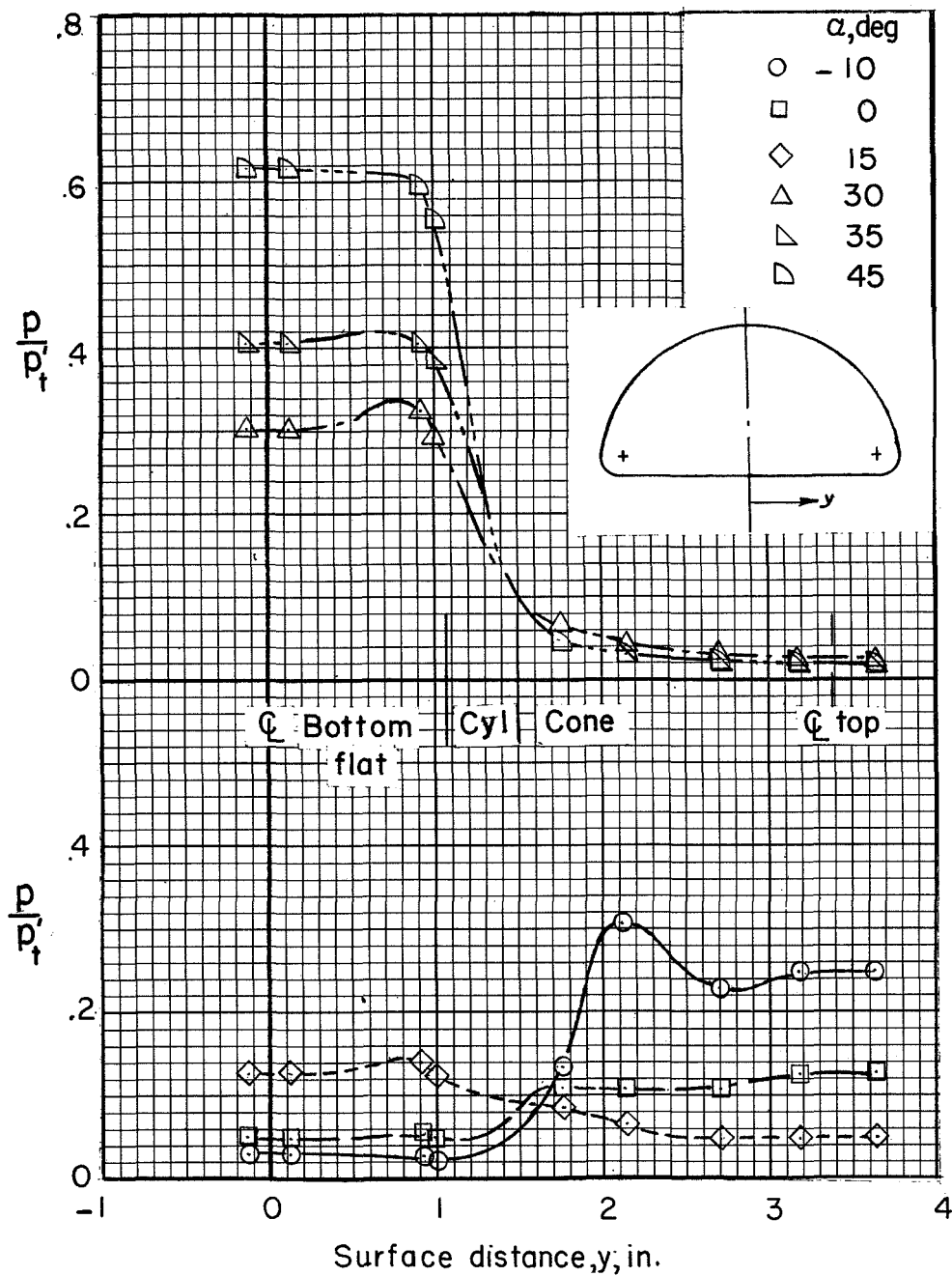
(a) $\alpha = -10^\circ$, 0° , and 15° .

Figure 3.- Pressure distribution along center line of model at several angles of attack.



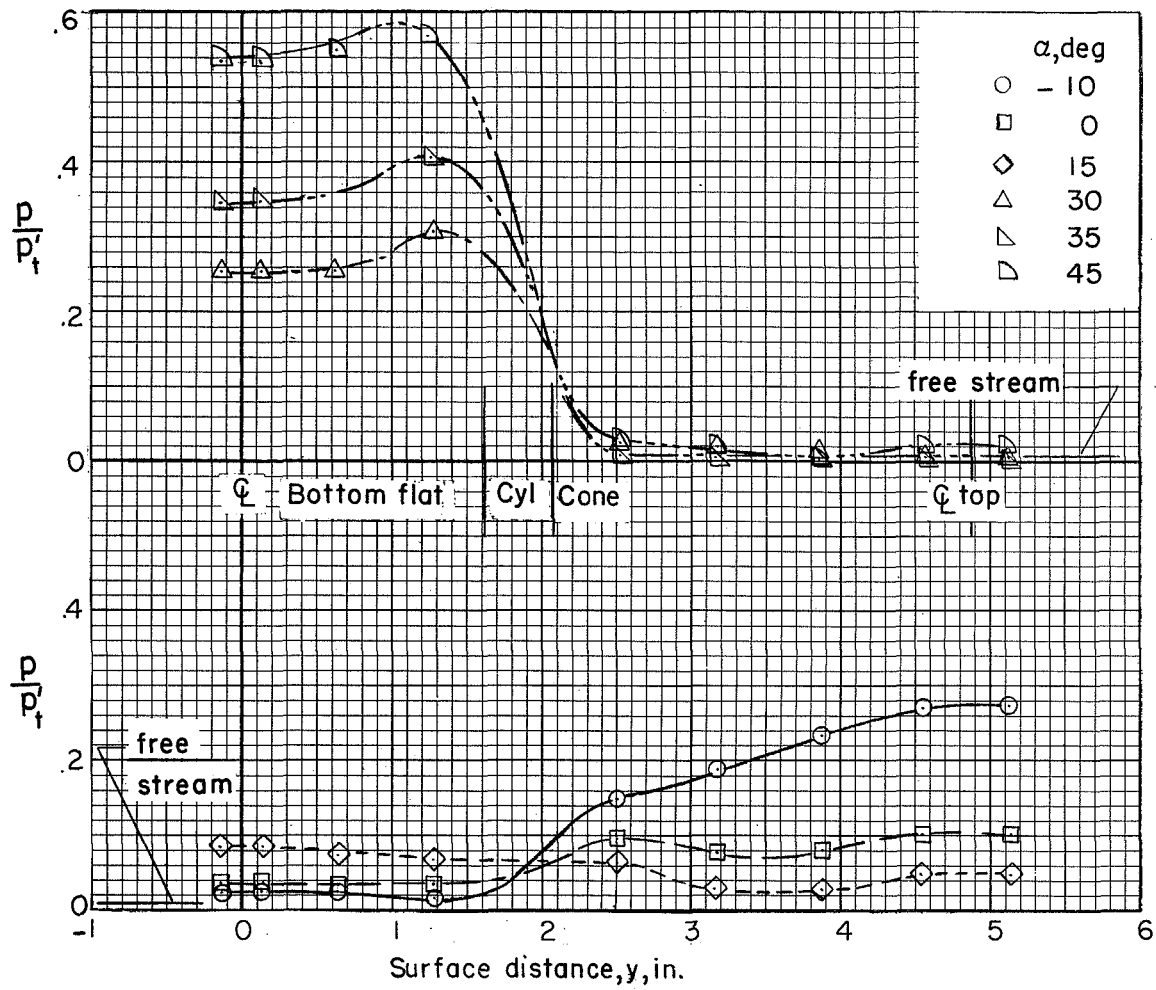
(b) $\alpha = 0^\circ, 30^\circ, 35^\circ, \text{ and } 45^\circ$.

Figure 3.- Concluded.



(a) Station 1.25.

Figure 4.- Transverse pressure distributions over the model at two stations for several angles of attack.



(b) Station 2.75.

Figure 4.- Concluded.

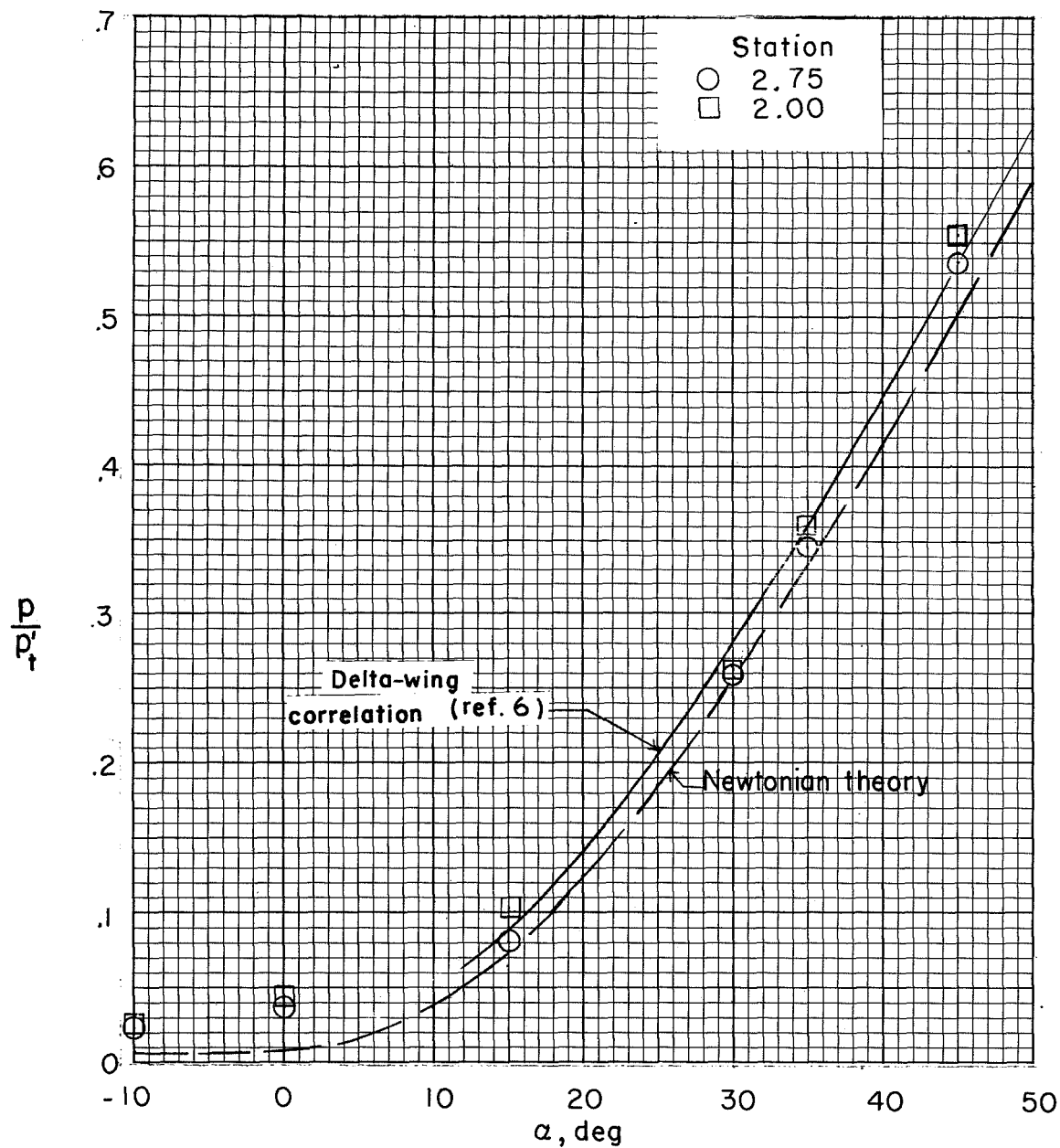
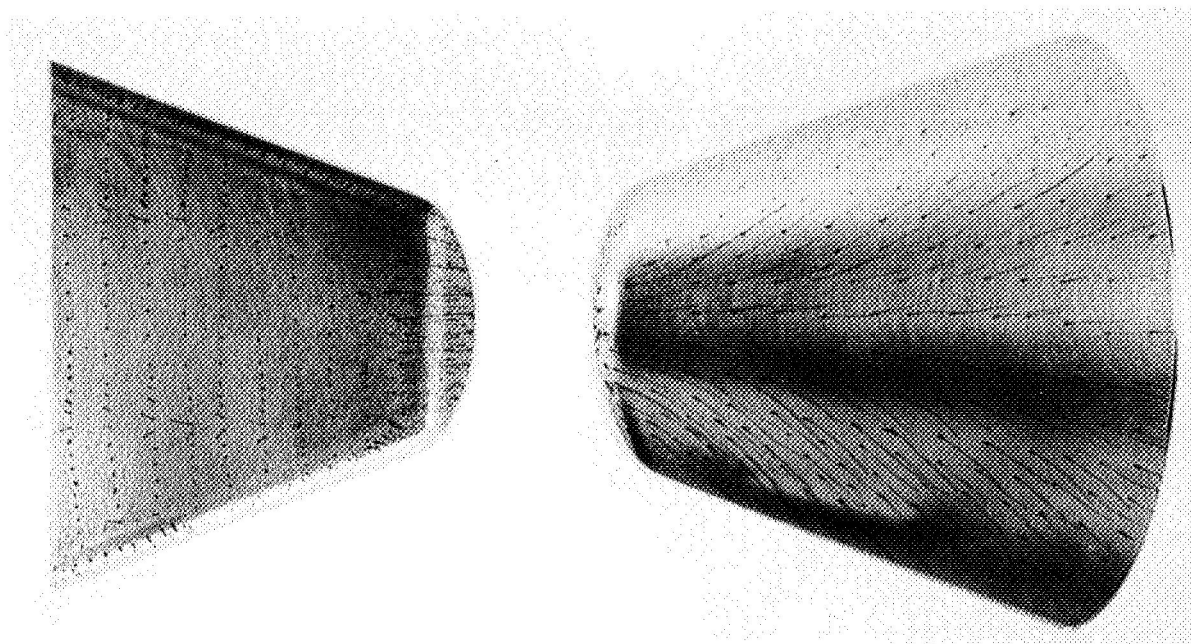
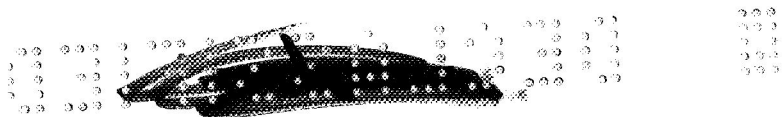
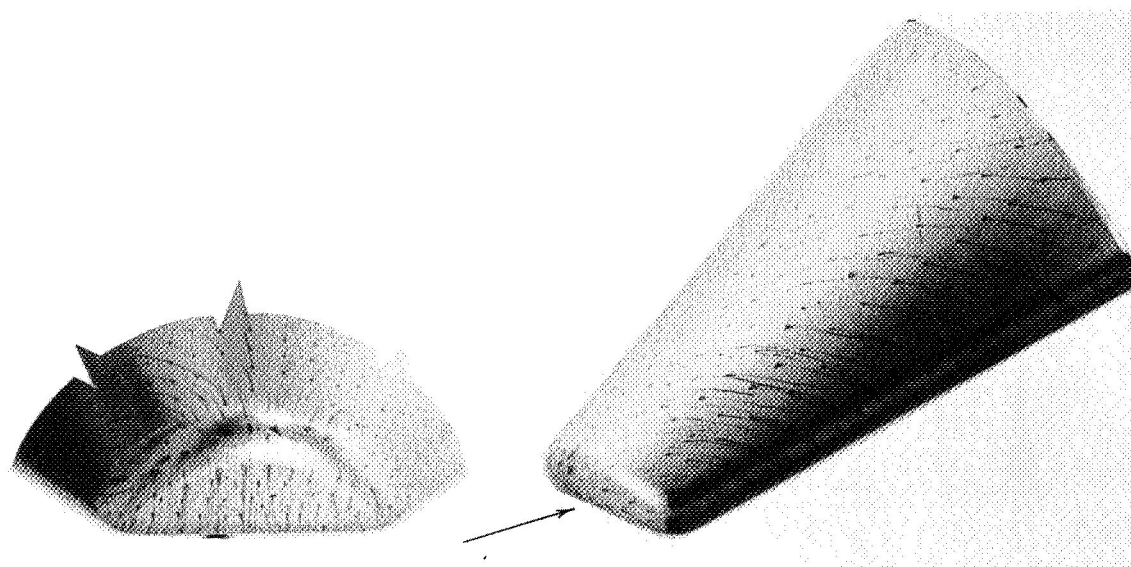


Figure 5.- Correlation of pressures obtained on flat bottom with pressures measured on delta wing and with Newtonian theory.



Bottom view

Top view



Front view

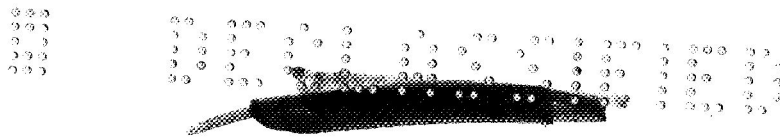
Side view

(a) $\alpha = -20^\circ$.

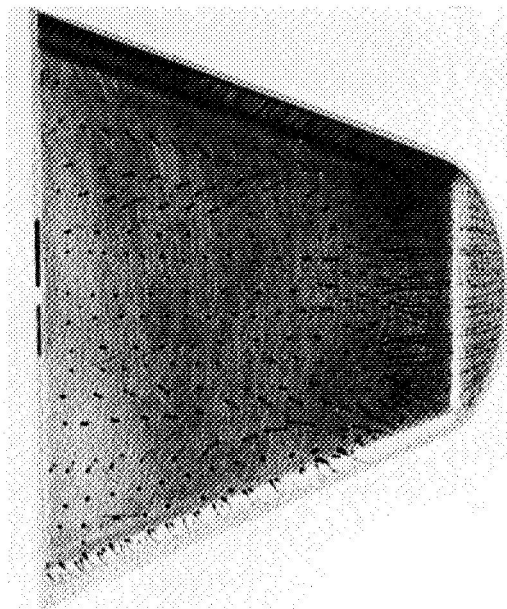
L-61-2229

Figure 6.- Surface oil-flow patterns. (Arrow indicates direction of free-stream flow.)

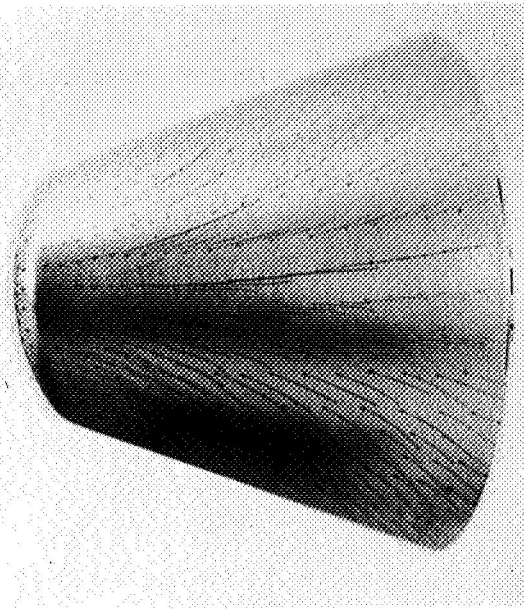




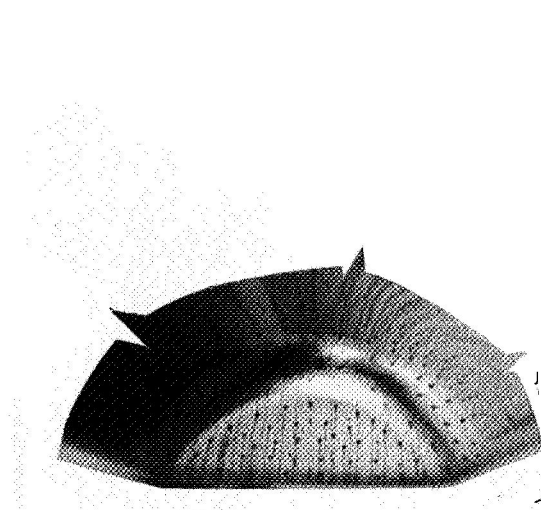
L-1602



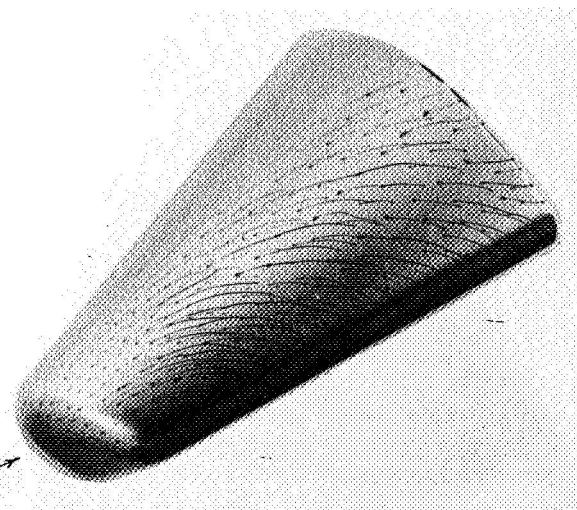
Bottom view



Top view



Front view



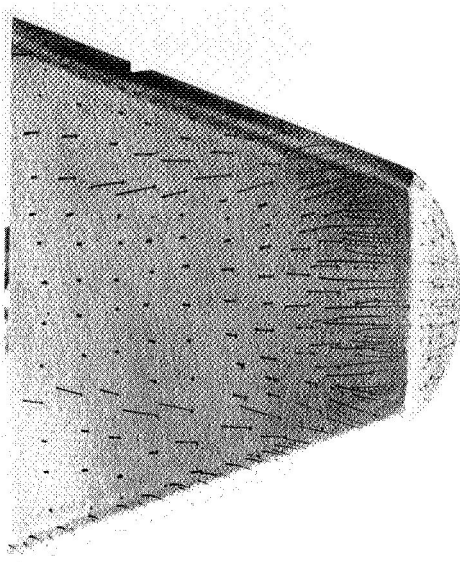
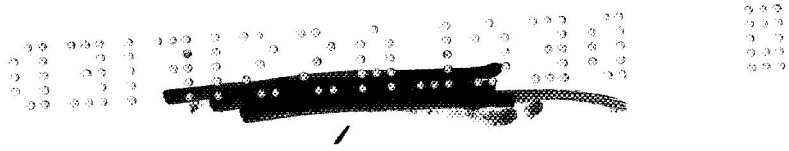
Side view

(b) $\alpha = -10^\circ$.

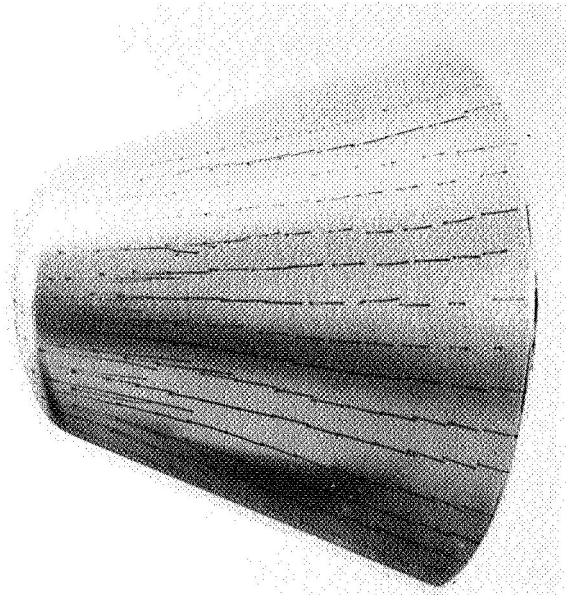
L-61-2230

Figure 6.- Continued.

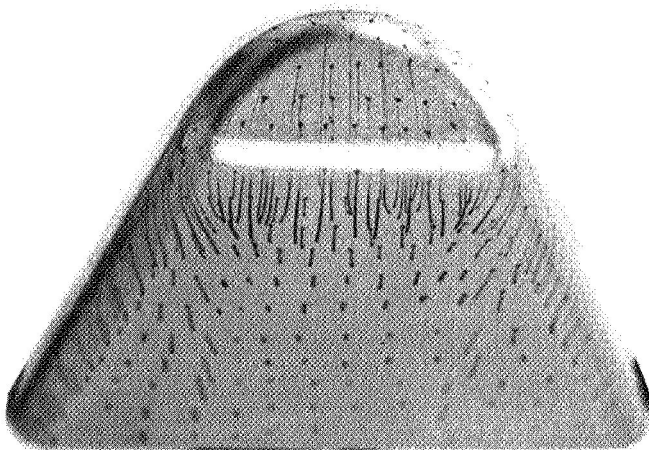




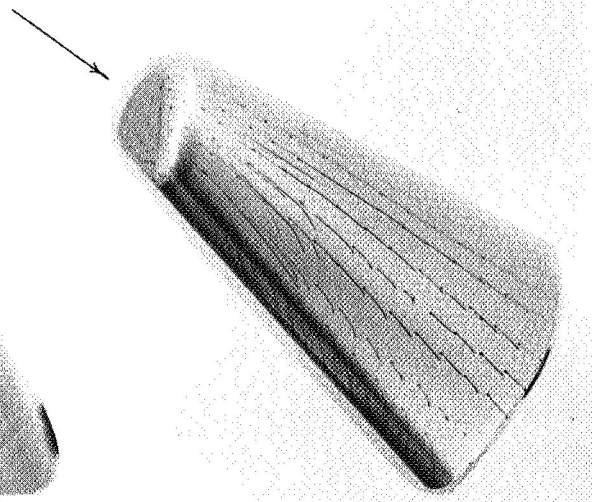
Bottom view



Top view



Front view



Side view

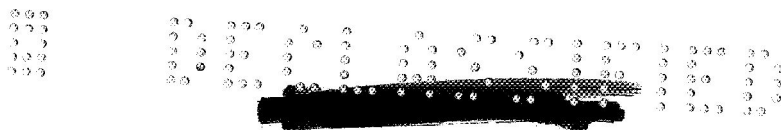
(c) $\alpha = 0^\circ$.

L-61-2231

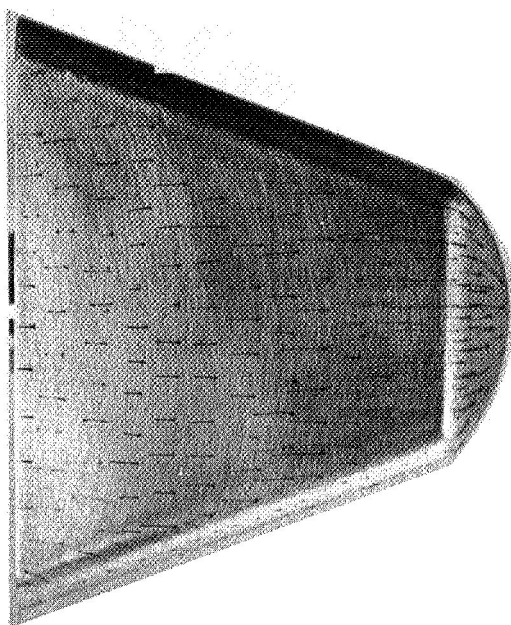
Figure 6.- Continued.



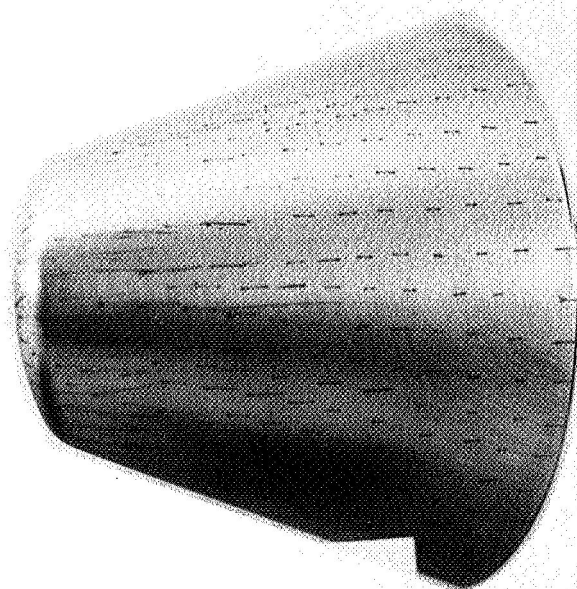
L-1602



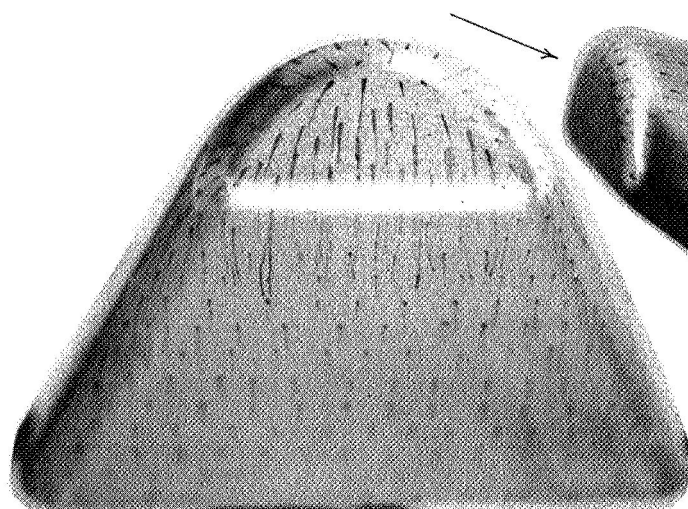
L-1602



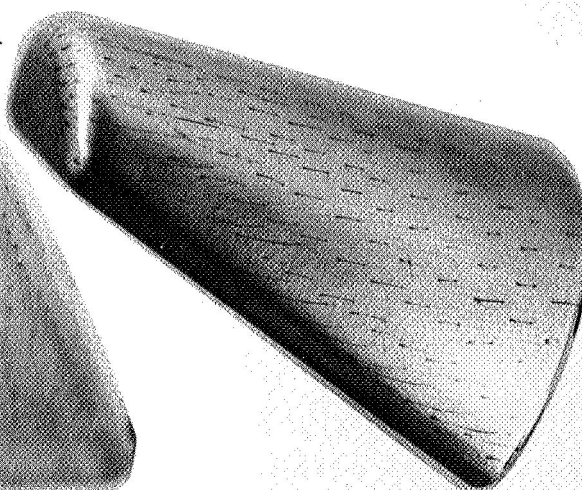
Bottom view



Top view



Front view



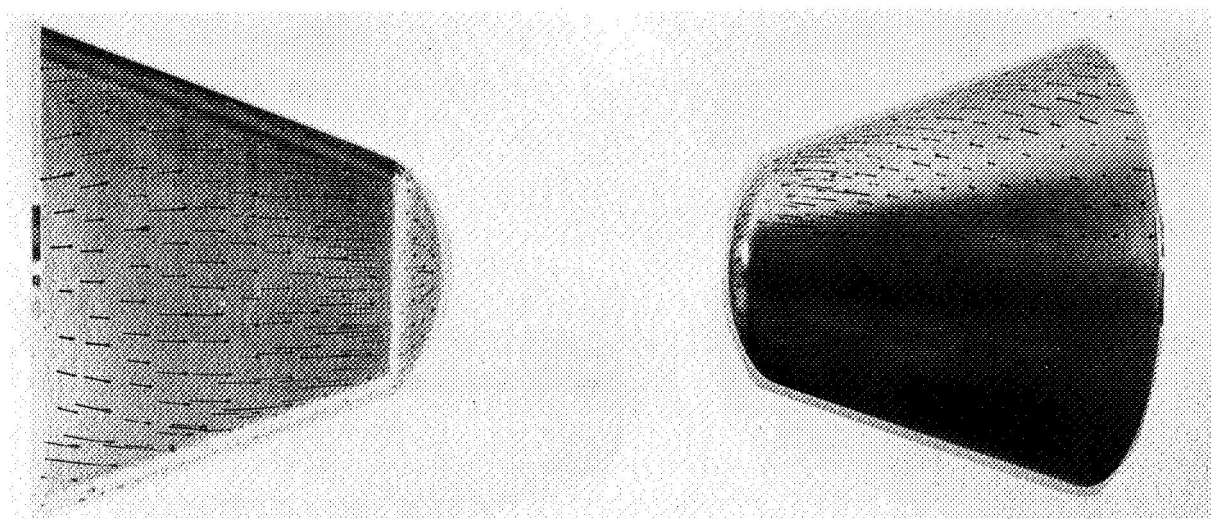
Side view

(d) $\alpha = 10^\circ$.

L-61-2232

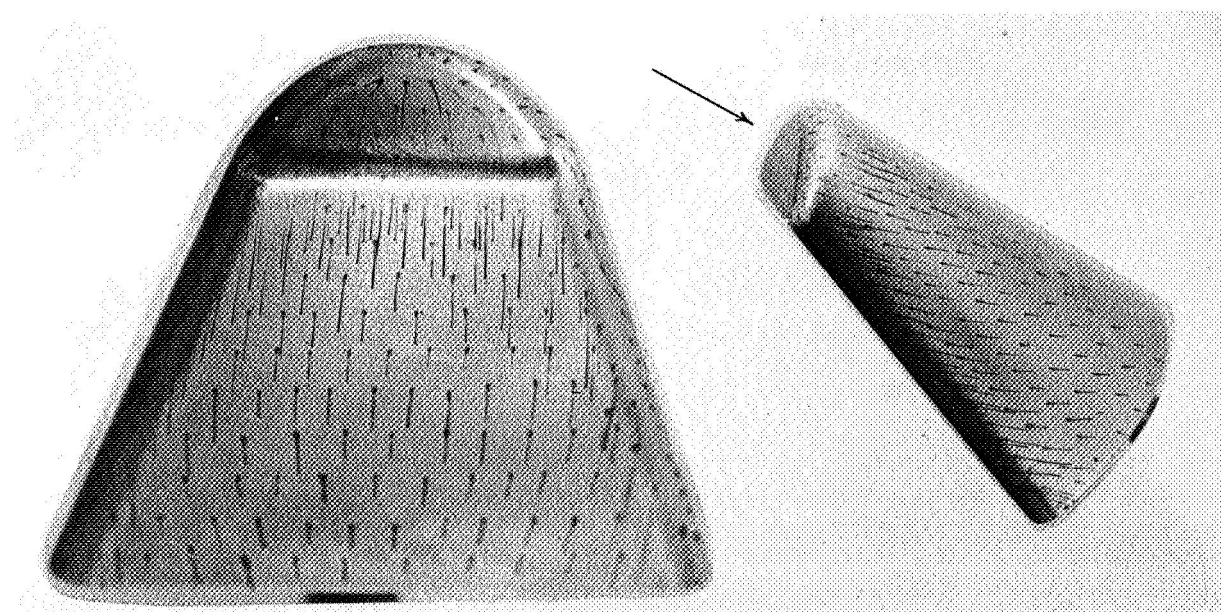
Figure 6.- Continued.





Bottom view

Top view



Front view

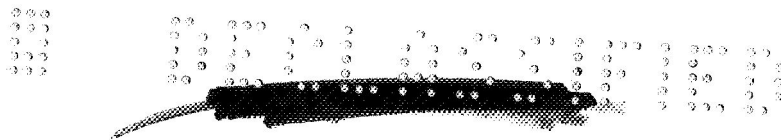
Side view

(e) $\alpha = 20^\circ$.

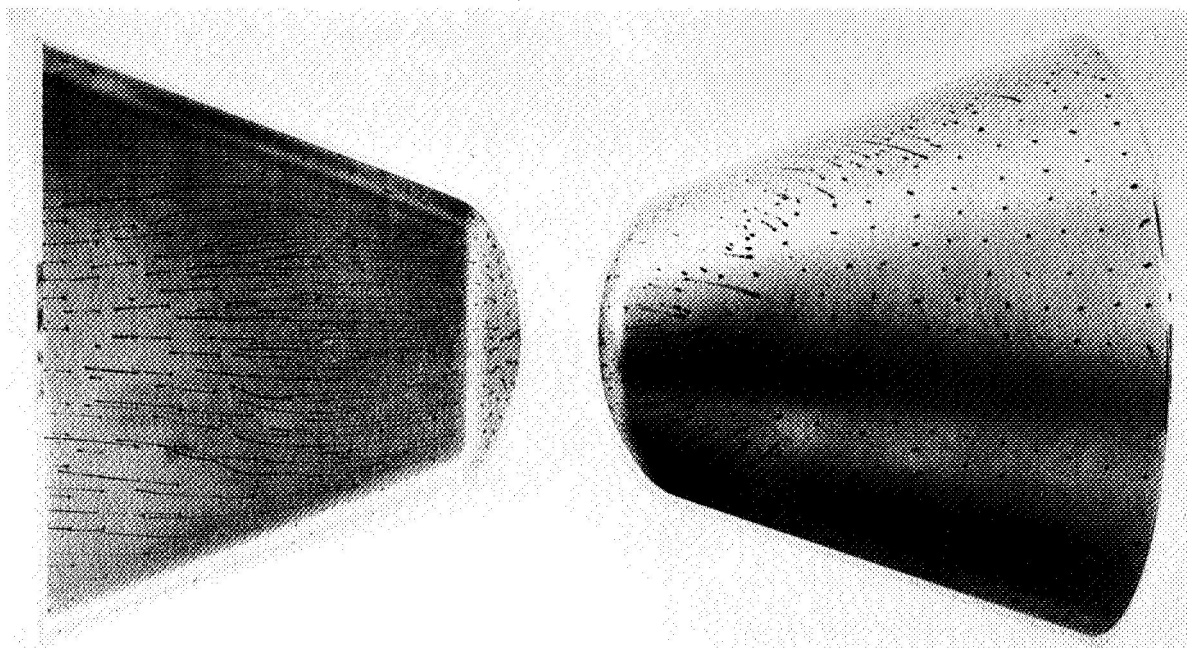
L-61-2233

Figure 6.- Continued.



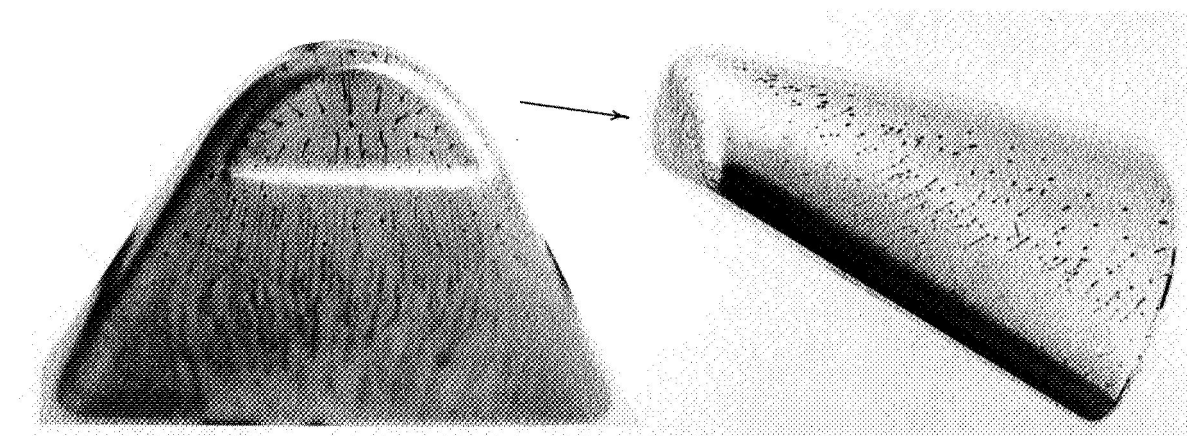


L-1602



Bottom view

Top view



Front view

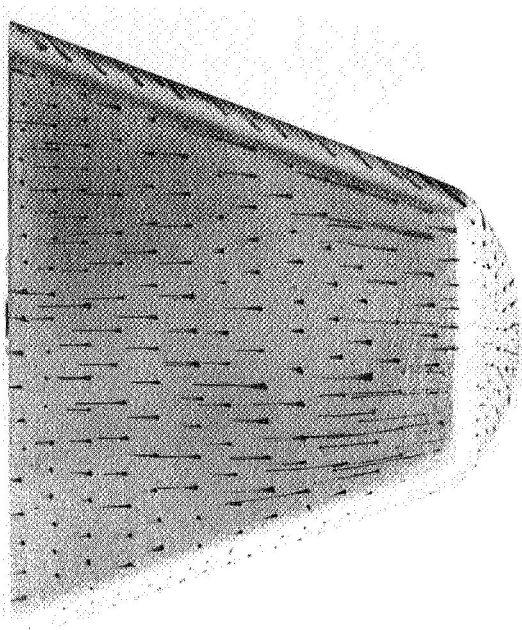
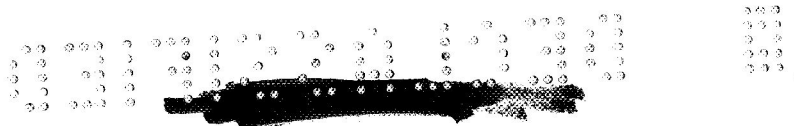
Side view

(f) $\alpha = 30^\circ$.

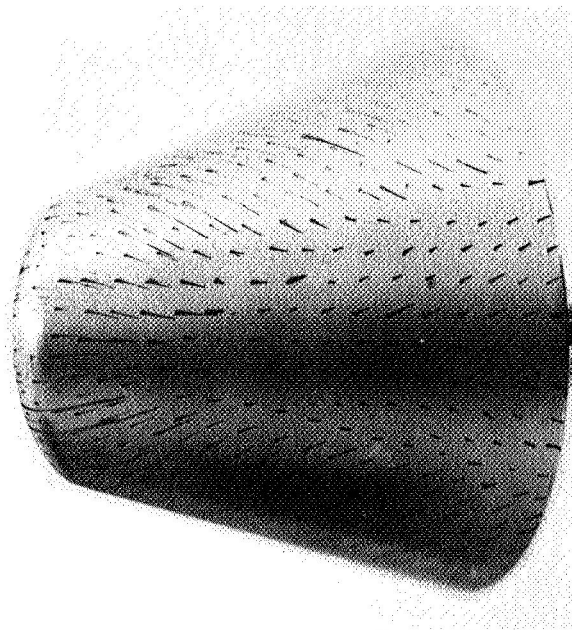
L-61-2234

Figure 6.- Continued.

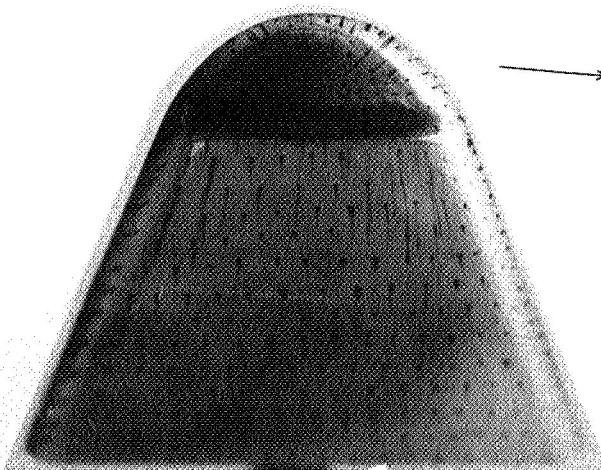




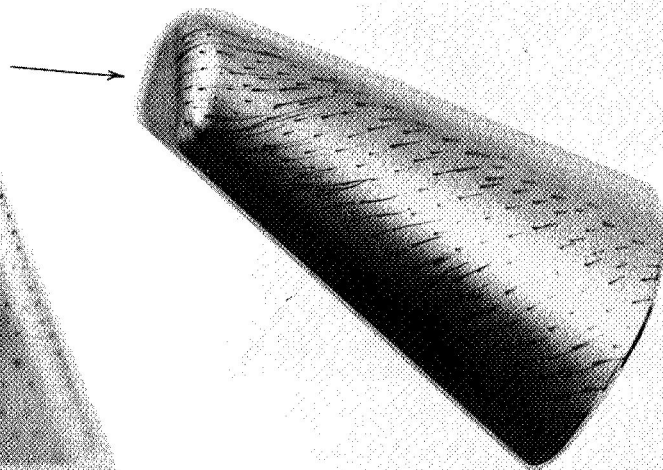
Bottom view



Top view



Front view



Side view

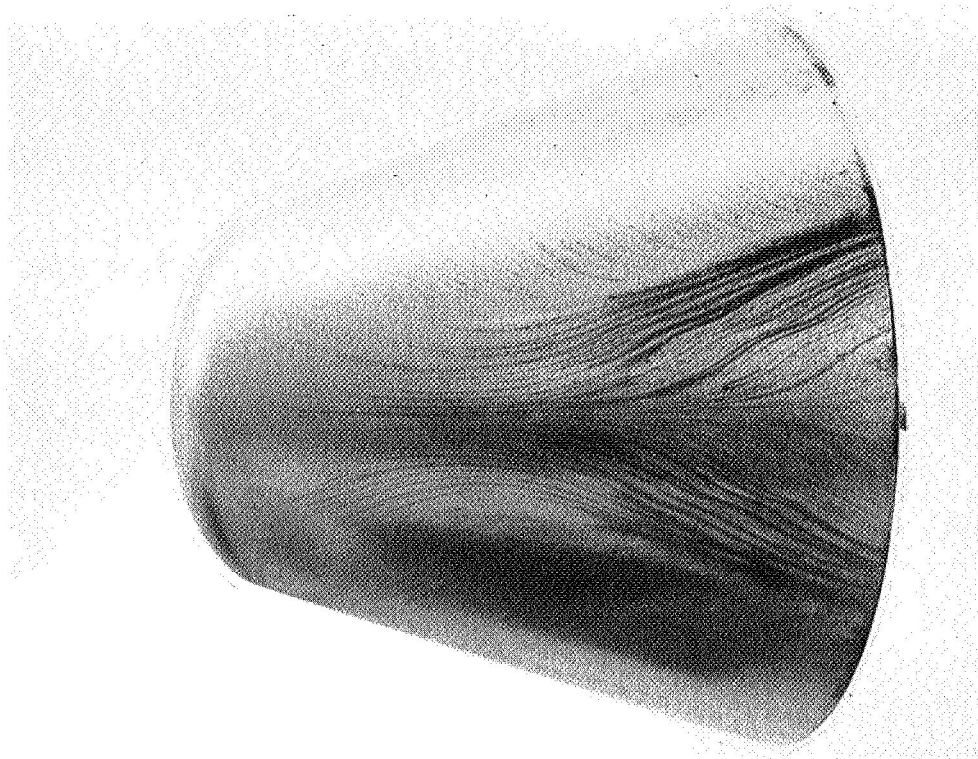
(g) $\alpha = 35^\circ$ (oil-dot technique).

L-61-2235

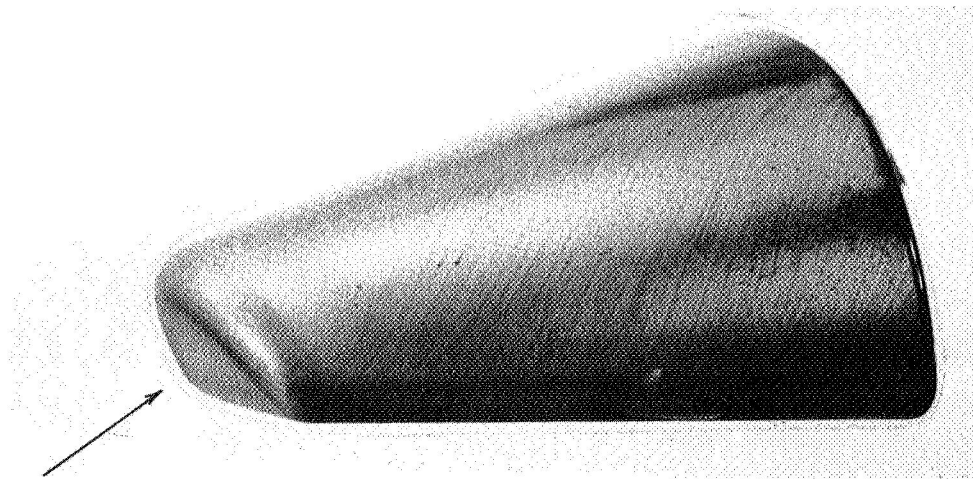
Figure 6.- Continued.

L-1602

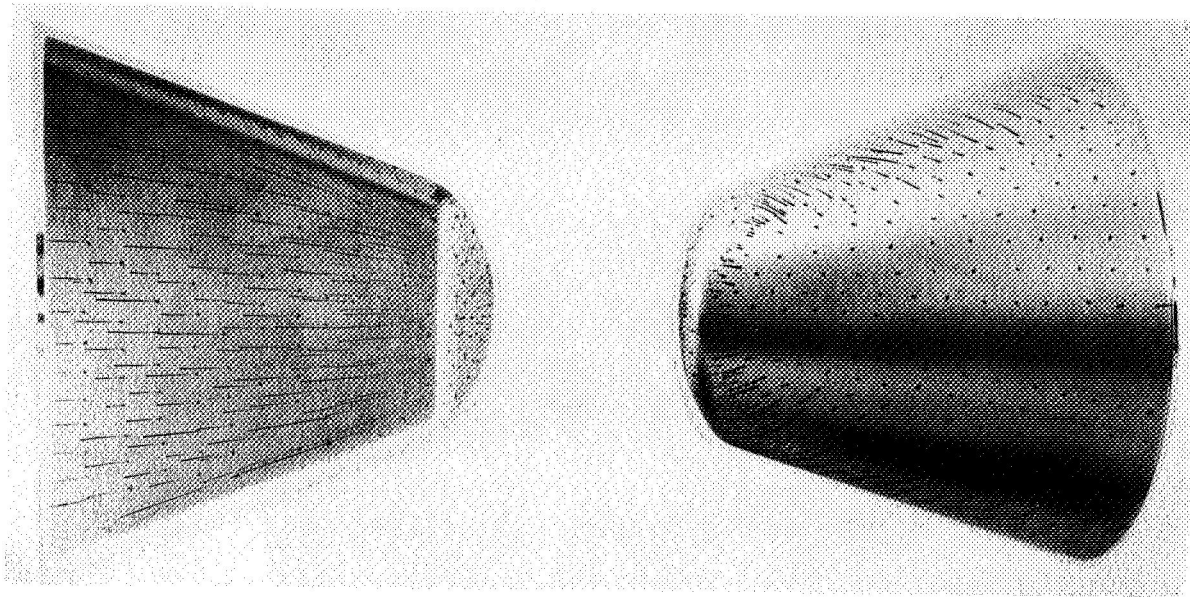
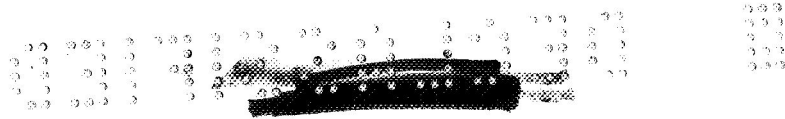
Figure 6.- Continued.



Top view

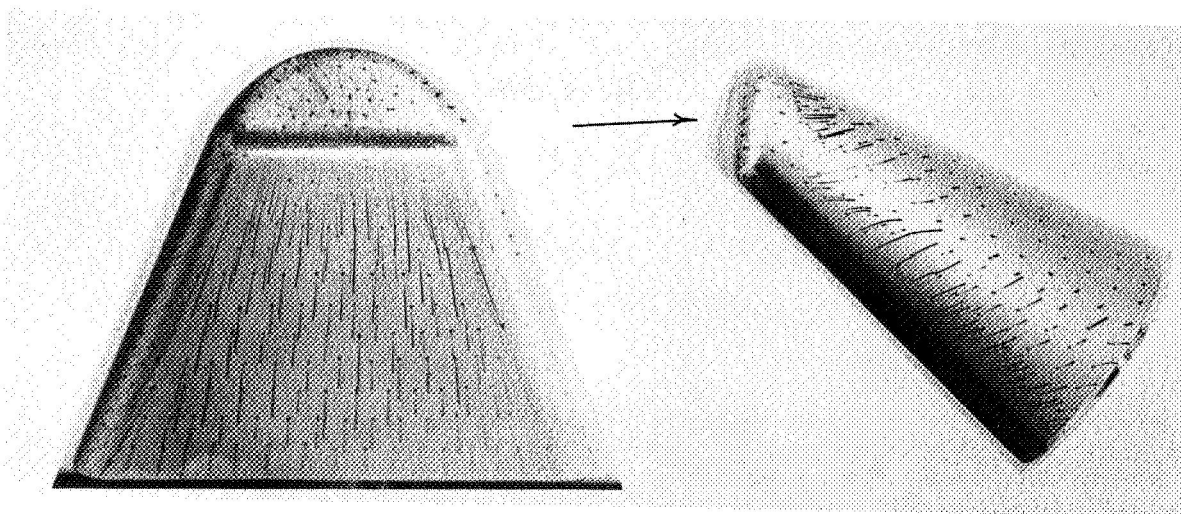


Side view



Bottom view

Top view



Front view

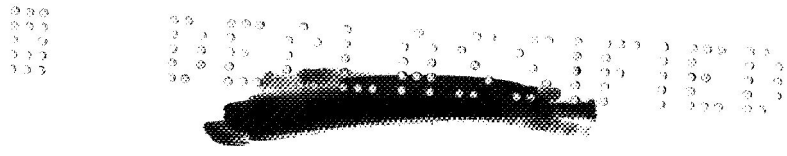
Side view

(1) $\alpha = 40^\circ$.

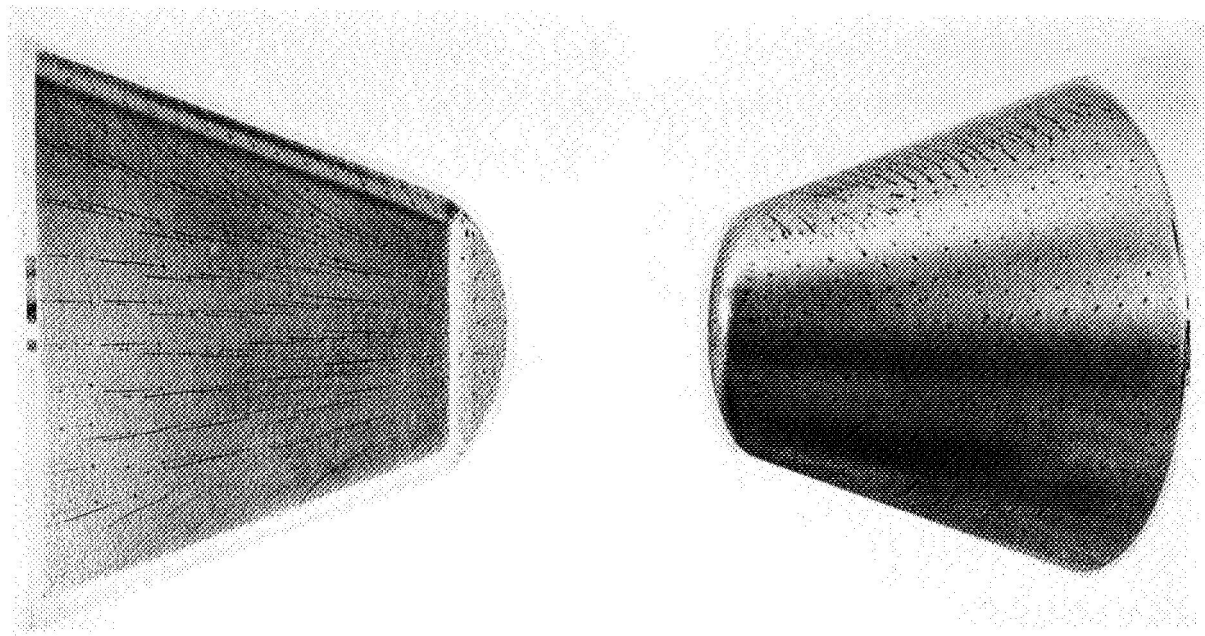
L-61-2237

Figure 6.- Continued.



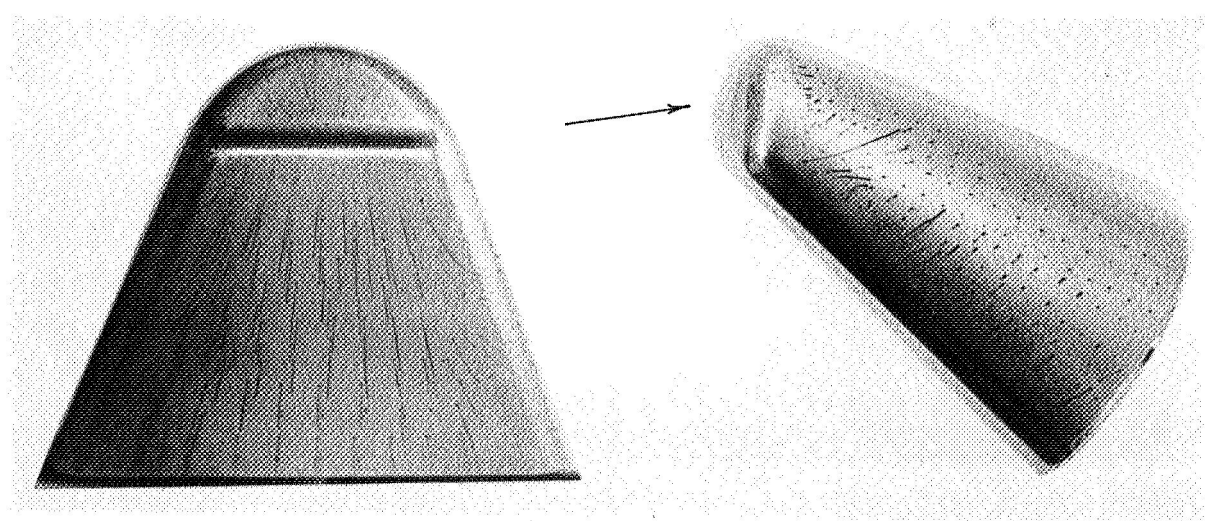


L-1602



Bottom view

Top view



Front view

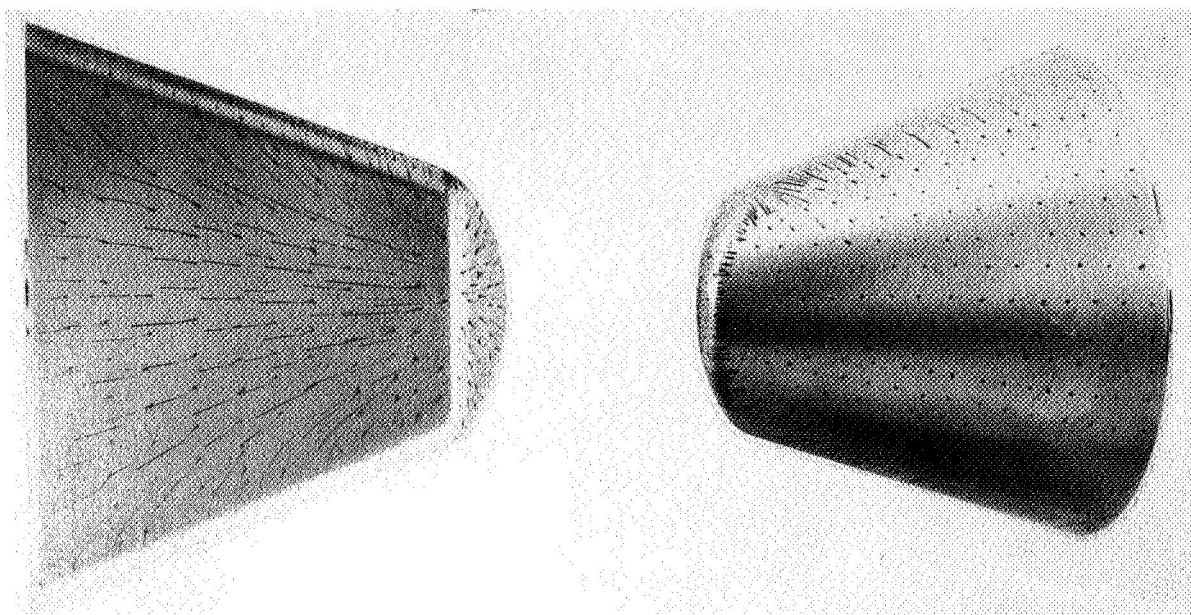
Side view

(j) $\alpha = 50^\circ$.

L-61-2238

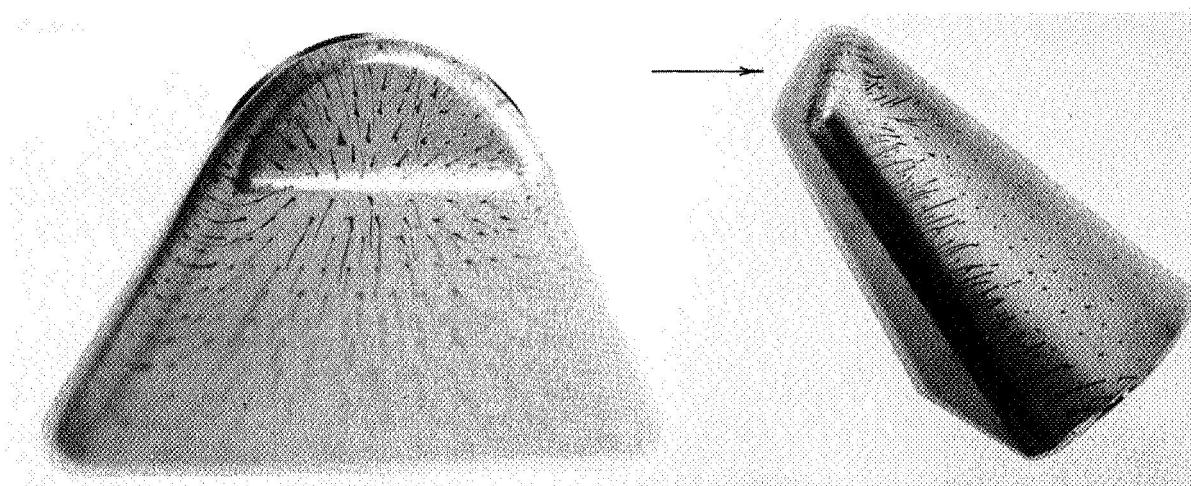
Figure 6.- Continued.





Bottom view

Top view



Front view

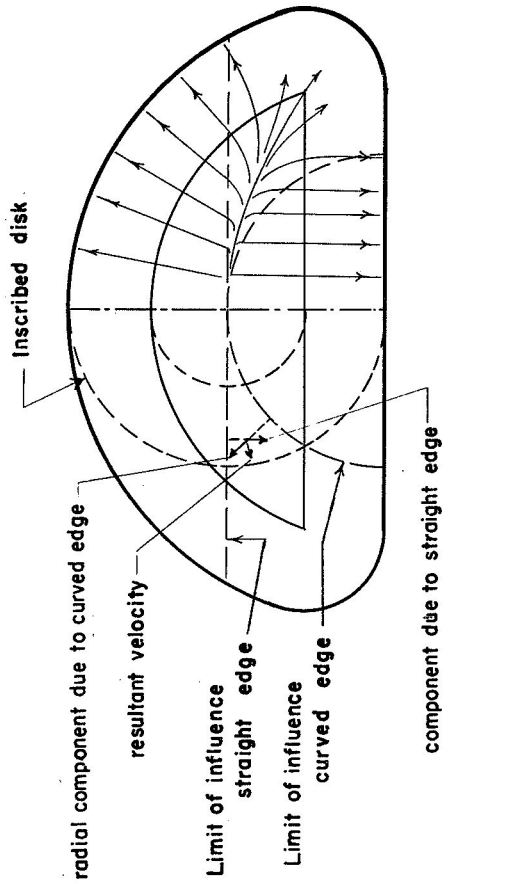
Side view

(k) $\alpha = 60^\circ$.

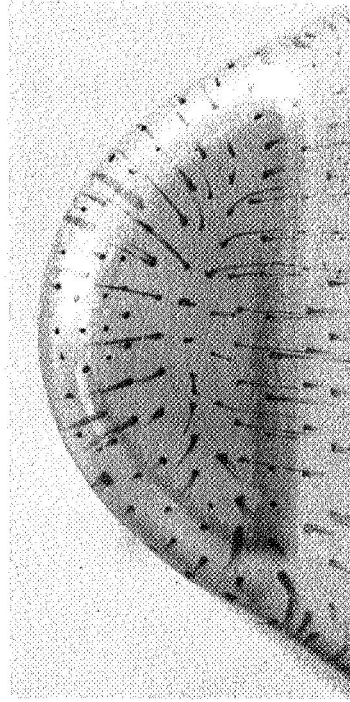
L-61-2239

Figure 6.- Concluded.

L-1602



(a) Construction of streamlines.



(b) Oil flow.

Figure 7.- Construction of inviscid streamlines by superposition of flows due to each edge.
 $\alpha = 35^\circ$ (nose flat normal to free stream).

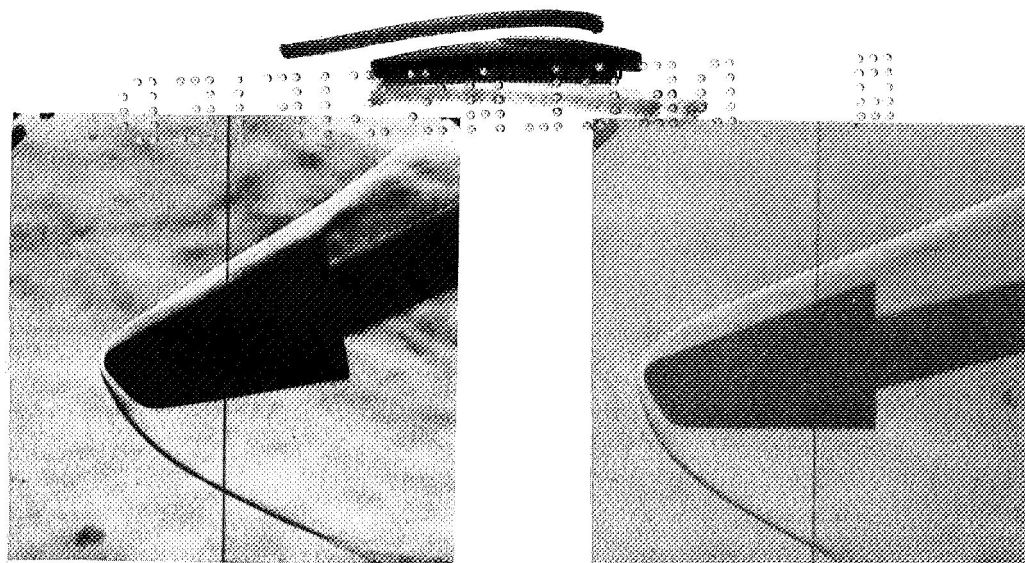
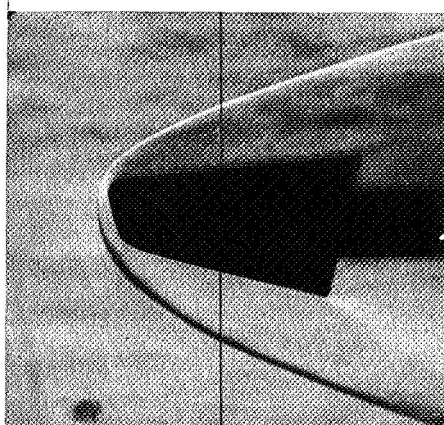
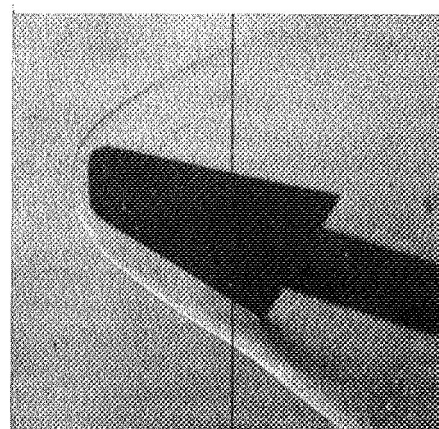
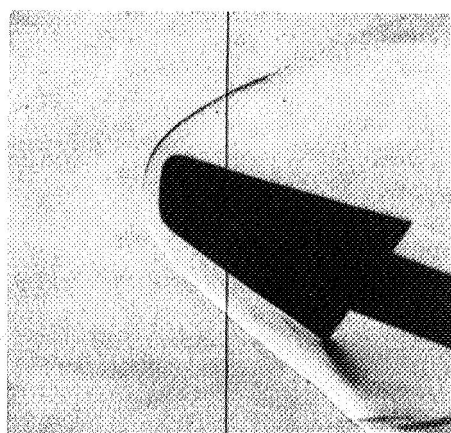
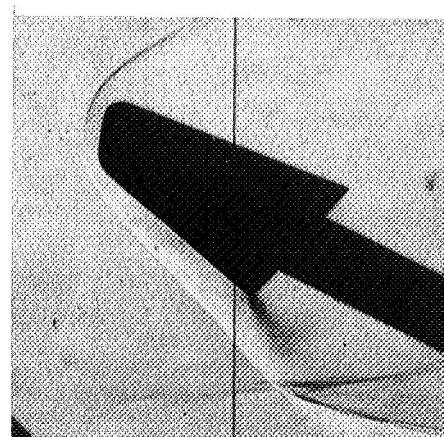
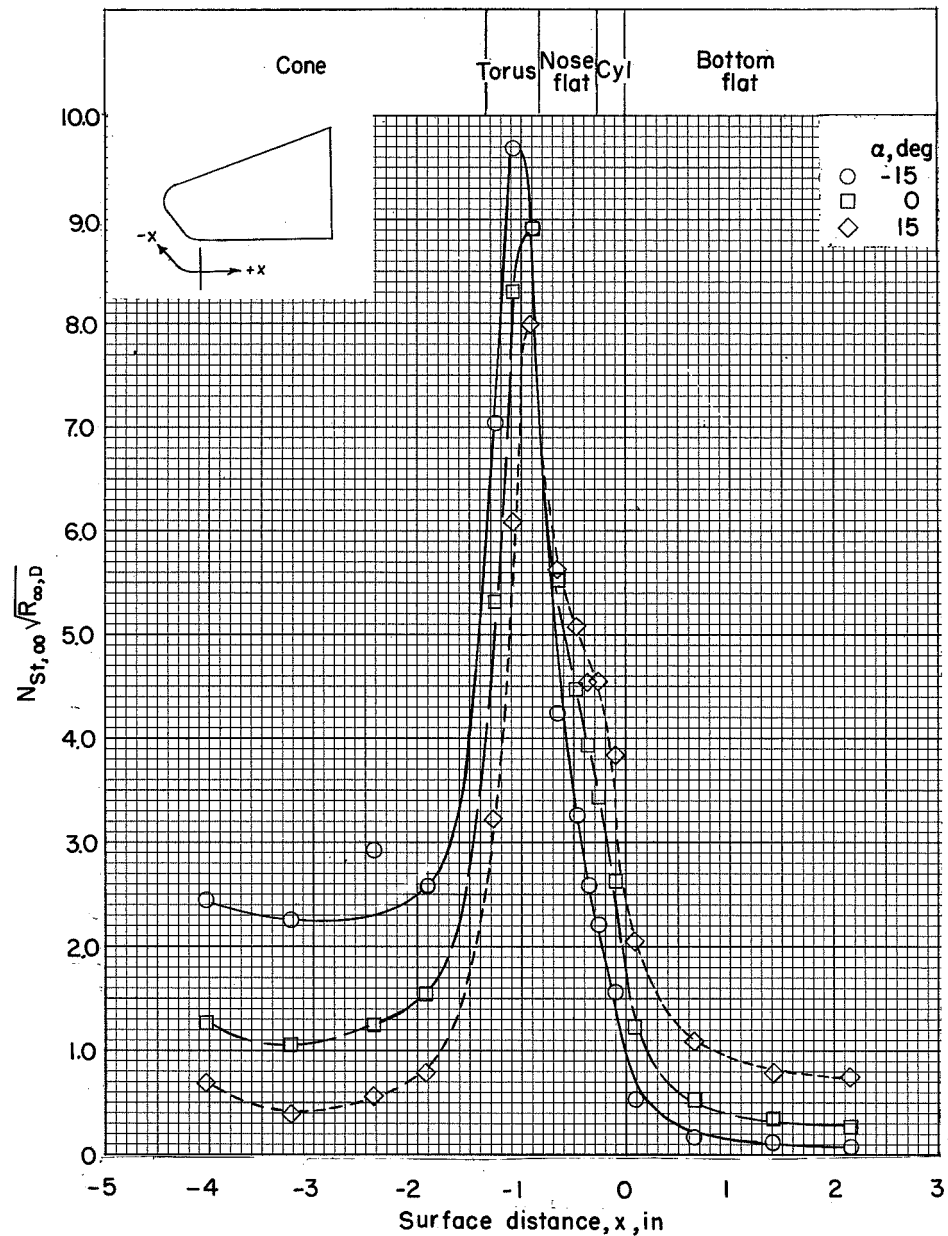
 $\alpha = -10^\circ$ $\alpha = 0^\circ$  $\alpha = 15^\circ$  $\alpha = 30^\circ$  $\alpha = 35^\circ$  $\alpha = 40^\circ$

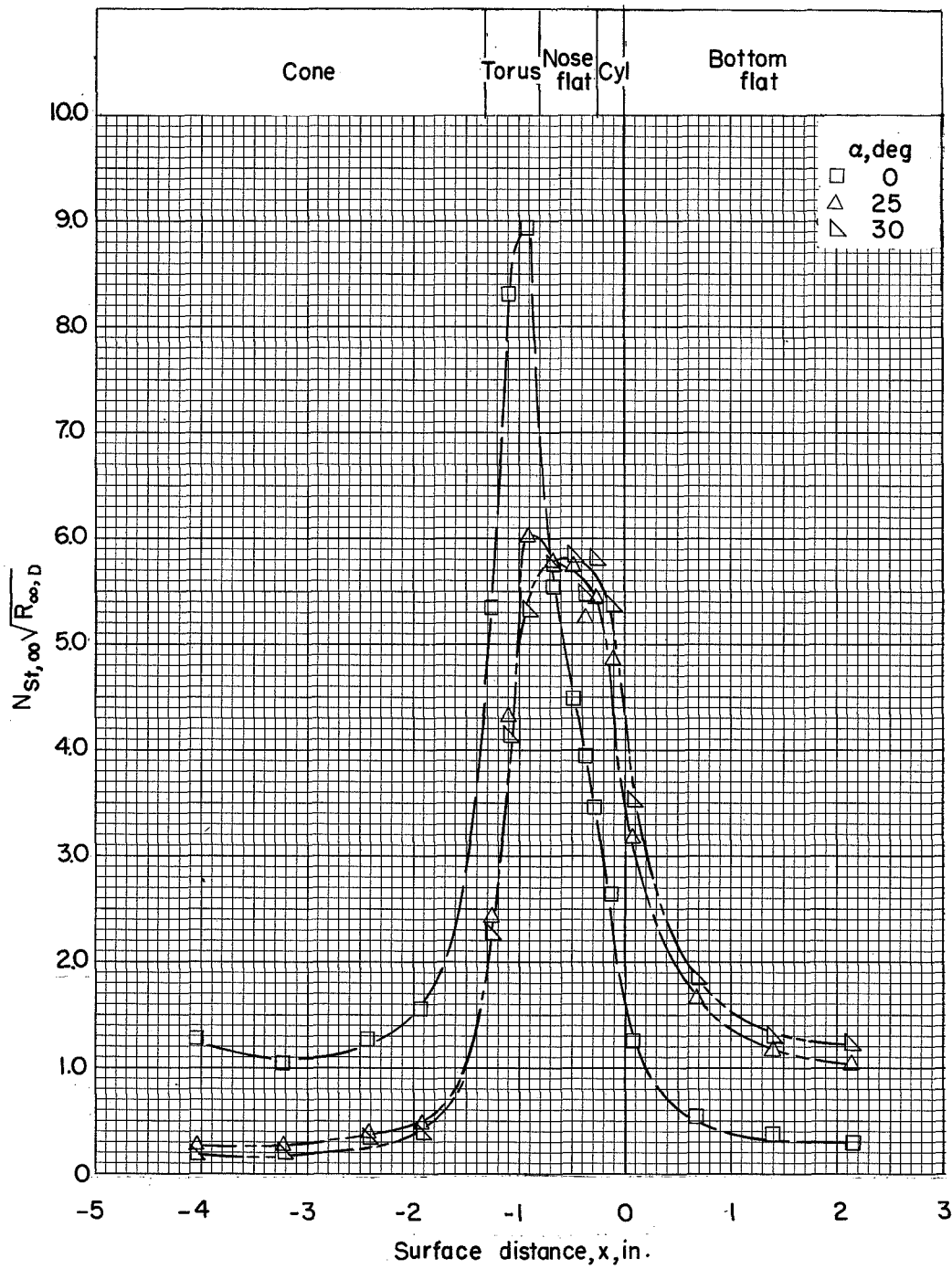
Figure 8.- Schlieren photographs for several angles of attack.

L-61-2241



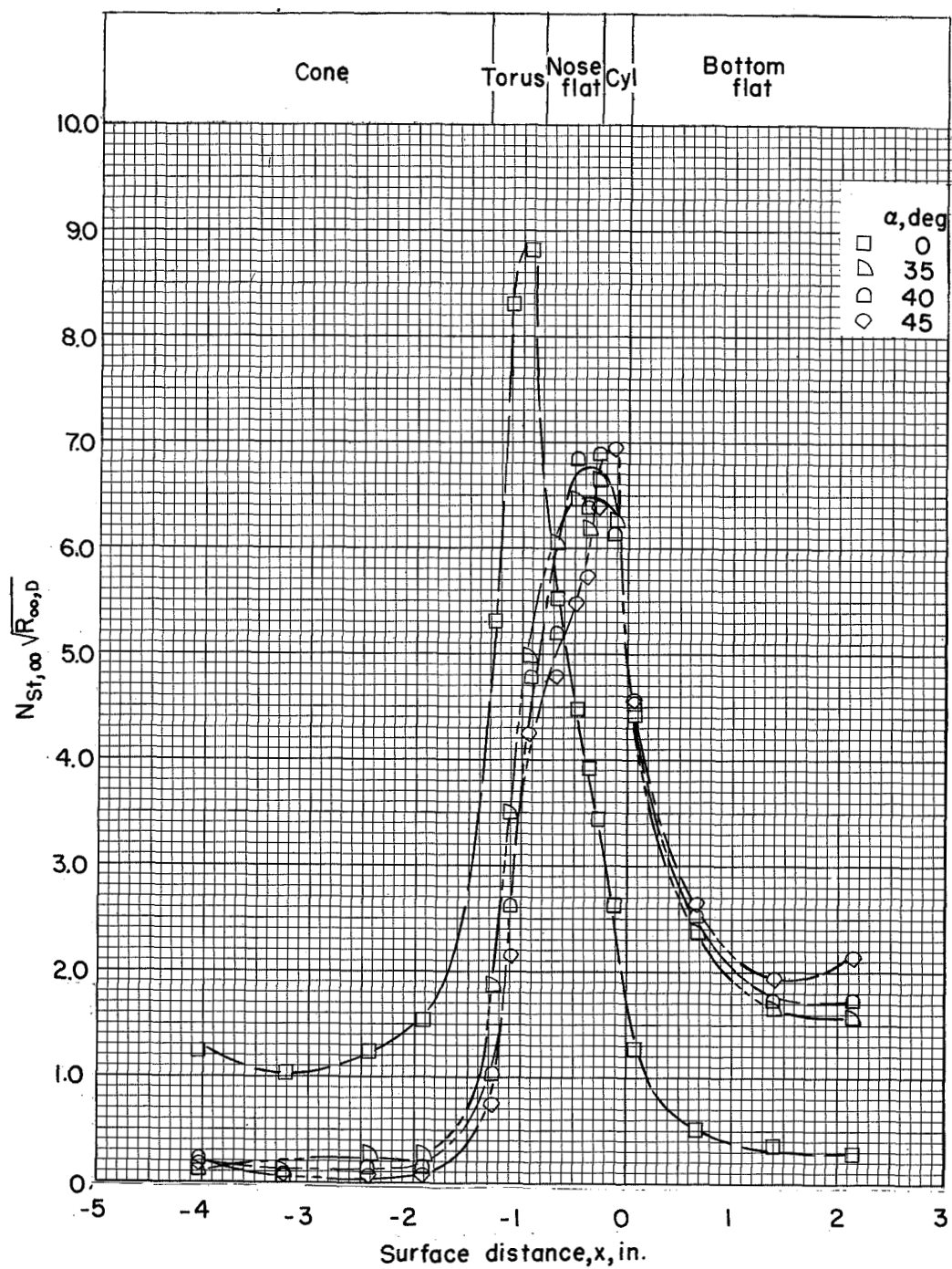
(a) $\alpha = -15^\circ, 0^\circ, \text{ and } 15^\circ$.

Figure 9.- Heat-transfer distribution along the center line of the model for several angles of attack. $M_\infty = 9.65$; $R_{\infty, D} = 0.118 \times 10^6$.



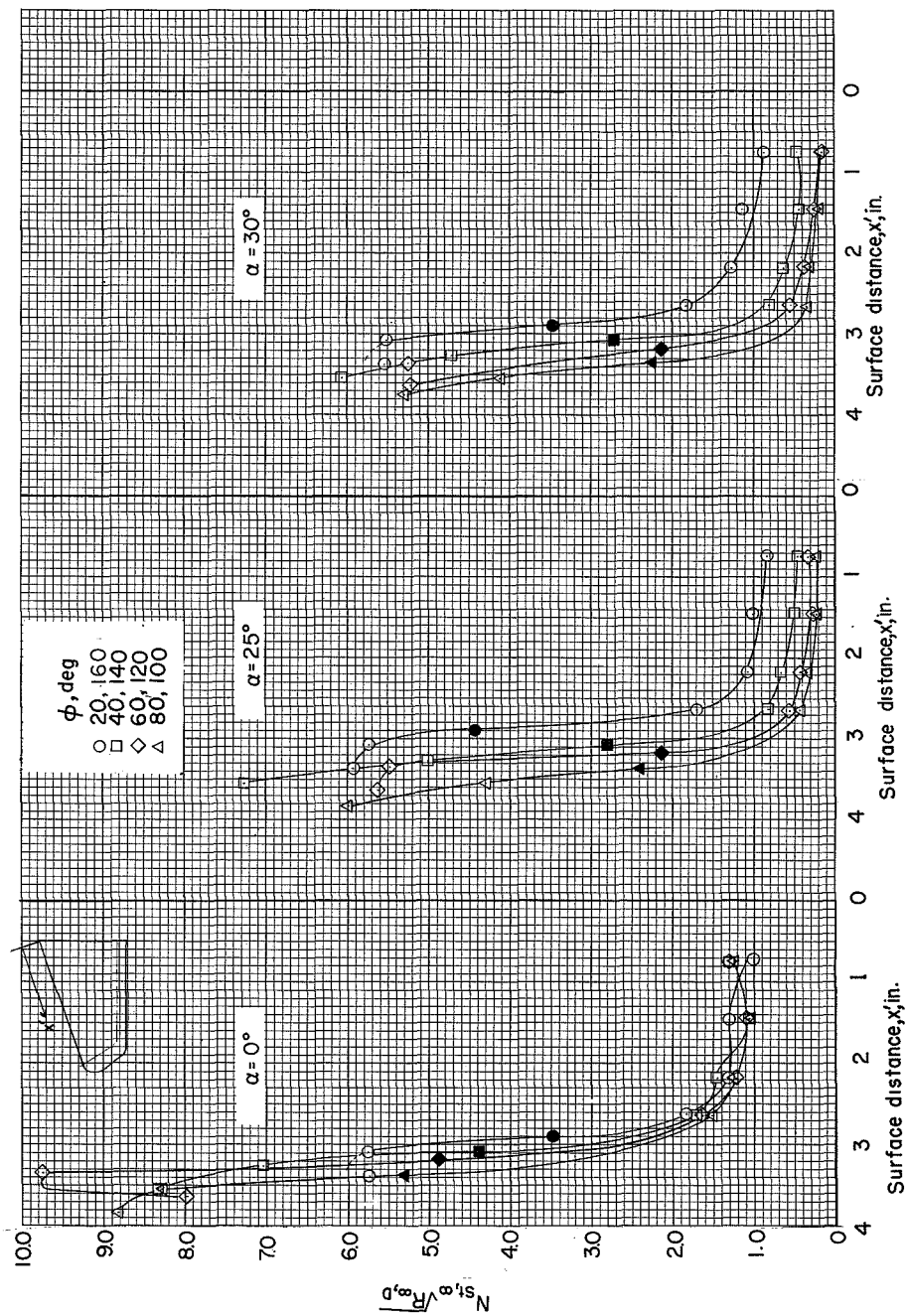
(b) $\alpha = 0^\circ, 25^\circ, \text{ and } 30^\circ.$

Figure 9.- Continued.



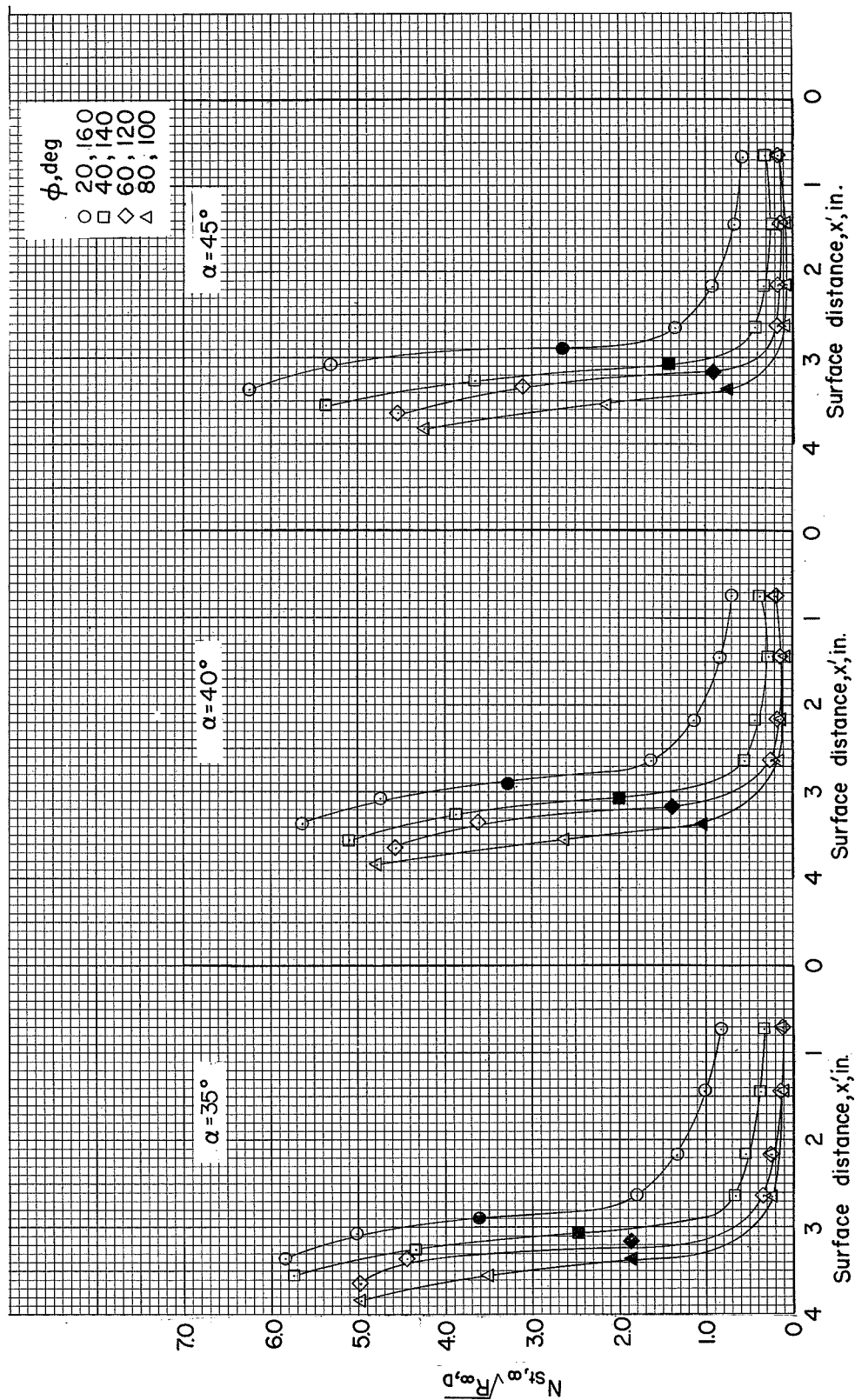
(c) $\alpha = 0^\circ, 35^\circ, 40^\circ$, and 45° .

Figure 9.- Concluded.



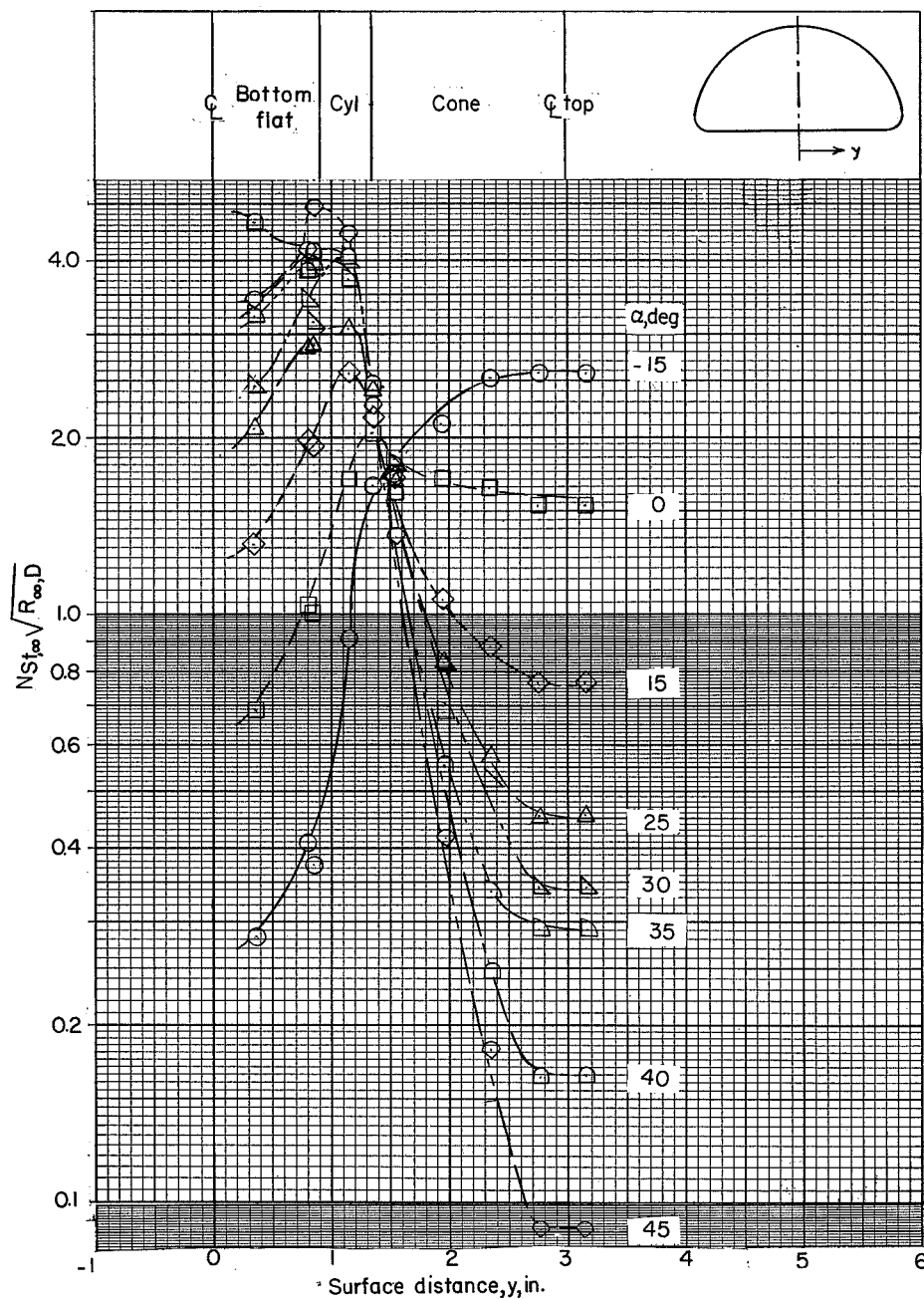
(a) $\alpha = 0^\circ, 25^\circ, \text{ and } 30^\circ$.

Figure 10.- Heat-transfer distribution over conical afterbody for several angles of attack. $M_\infty = 9.65$; $R_{\infty, D} = 0.118 \times 10^6$. (Solid symbol denotes point of tangency between toroidal surface and conical afterbody.)



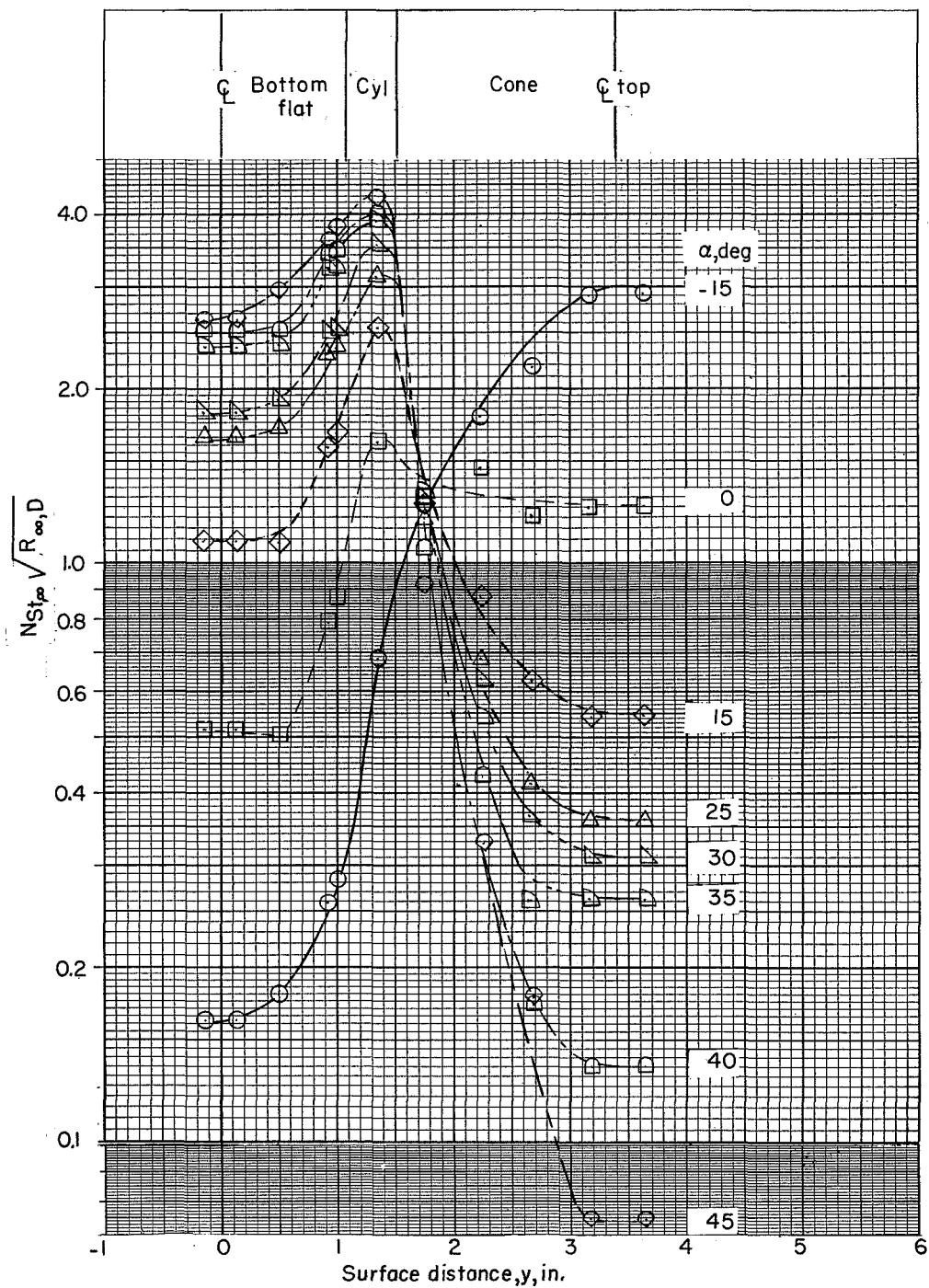
(b) $\alpha = 35^\circ, 40^\circ, \text{ and } 45^\circ.$

Figure 10.- Concluded.



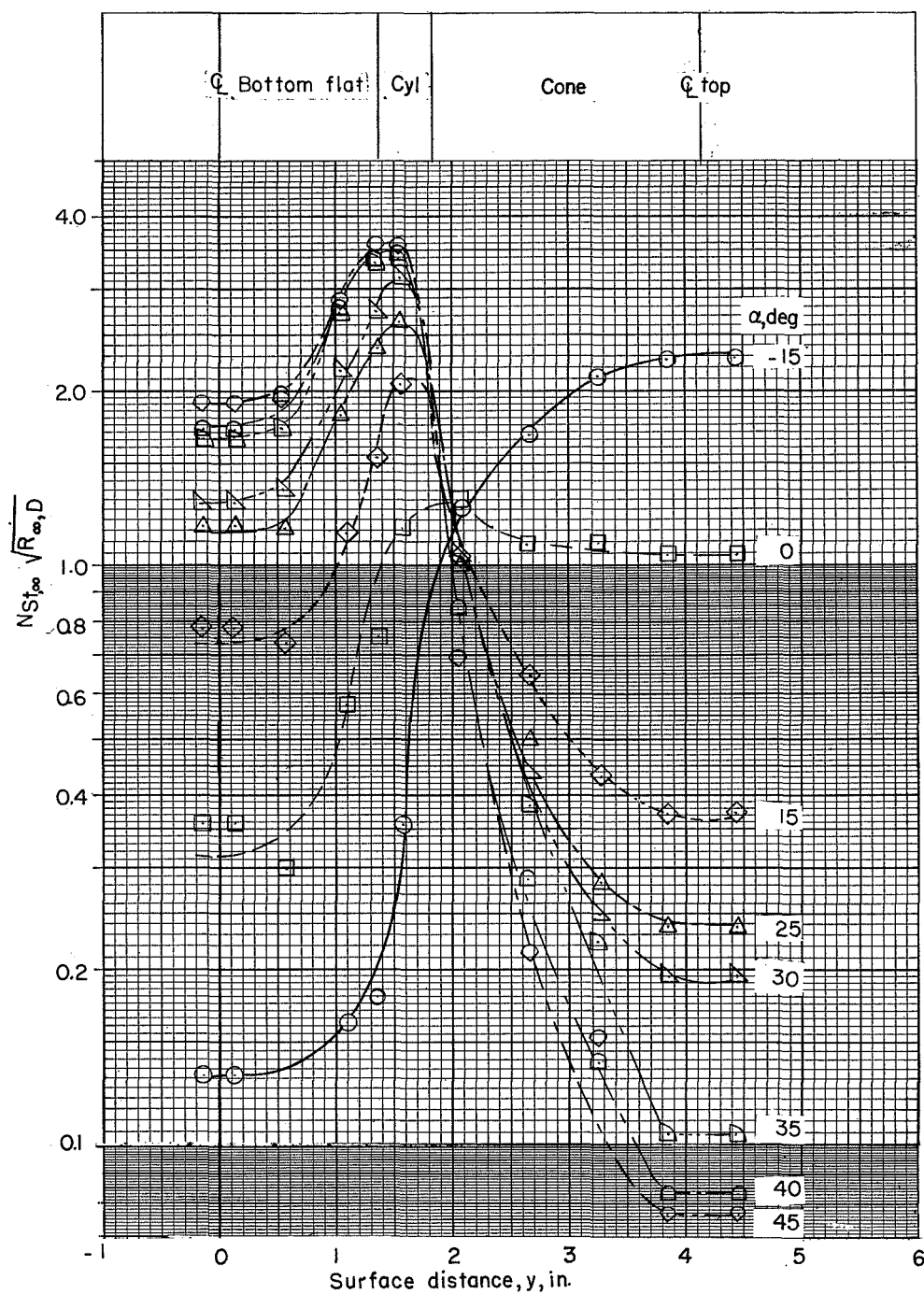
(a) Station 0.875.

Figure 11.- Circumferential heat-transfer distribution with angle of attack at several stations on the model. $M_{\infty} = 9.65$; $R_{\infty, D} = 0.118 \times 10^6$.



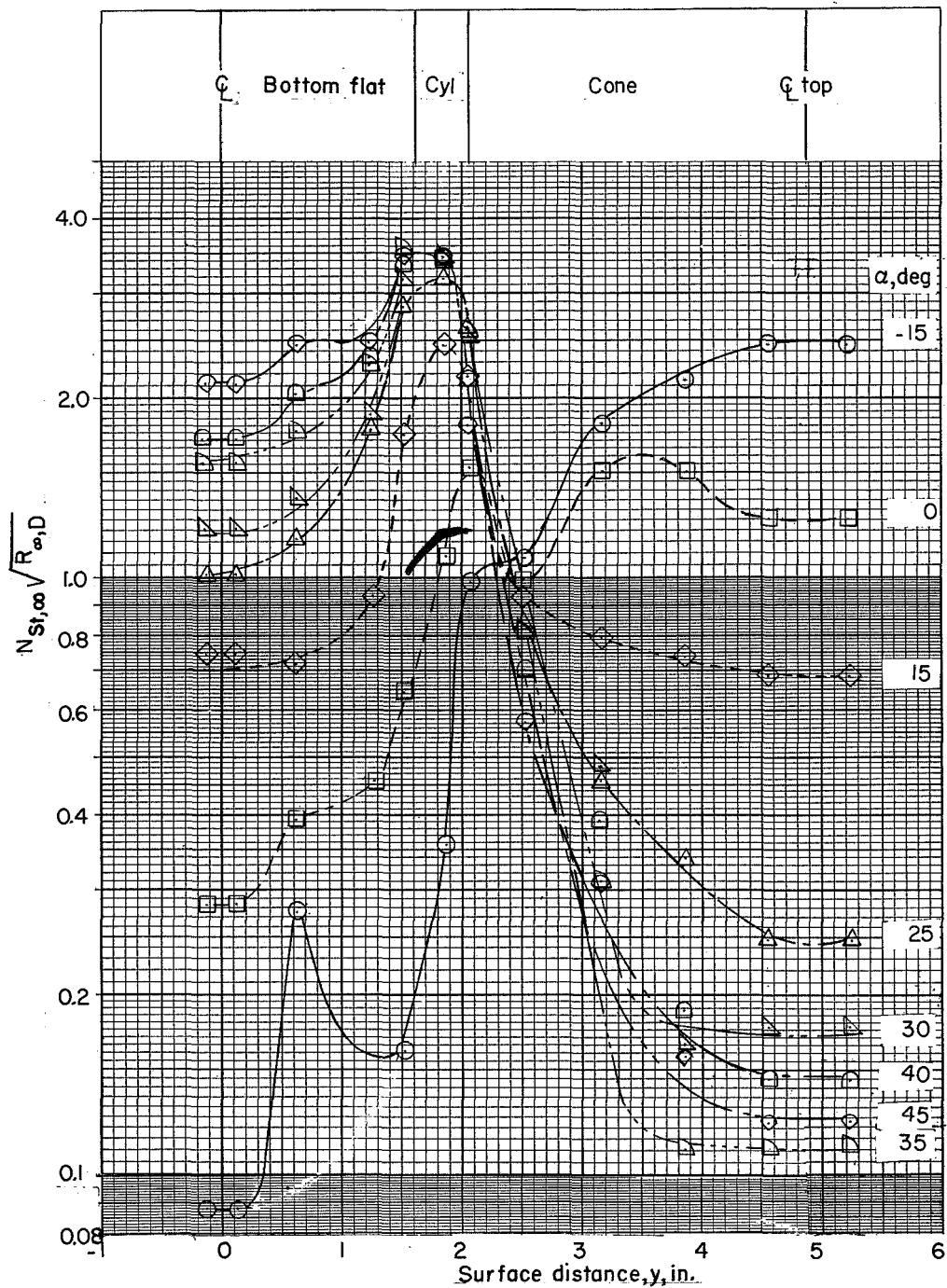
(b) Station 1.25.

Figure 11.- Continued.



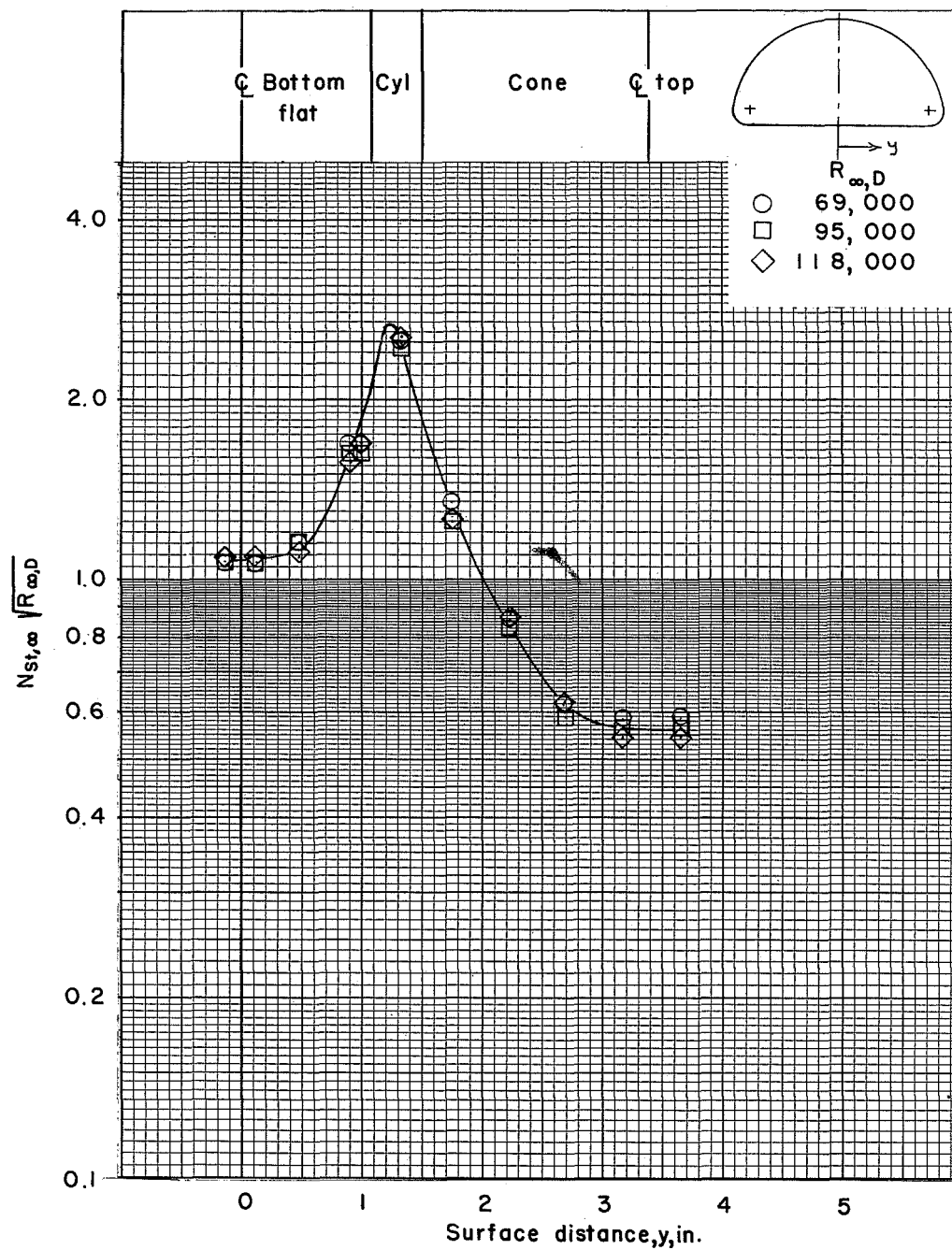
(c) Station 2.00.

Figure 11.- Continued.



(d) Station 2.75.

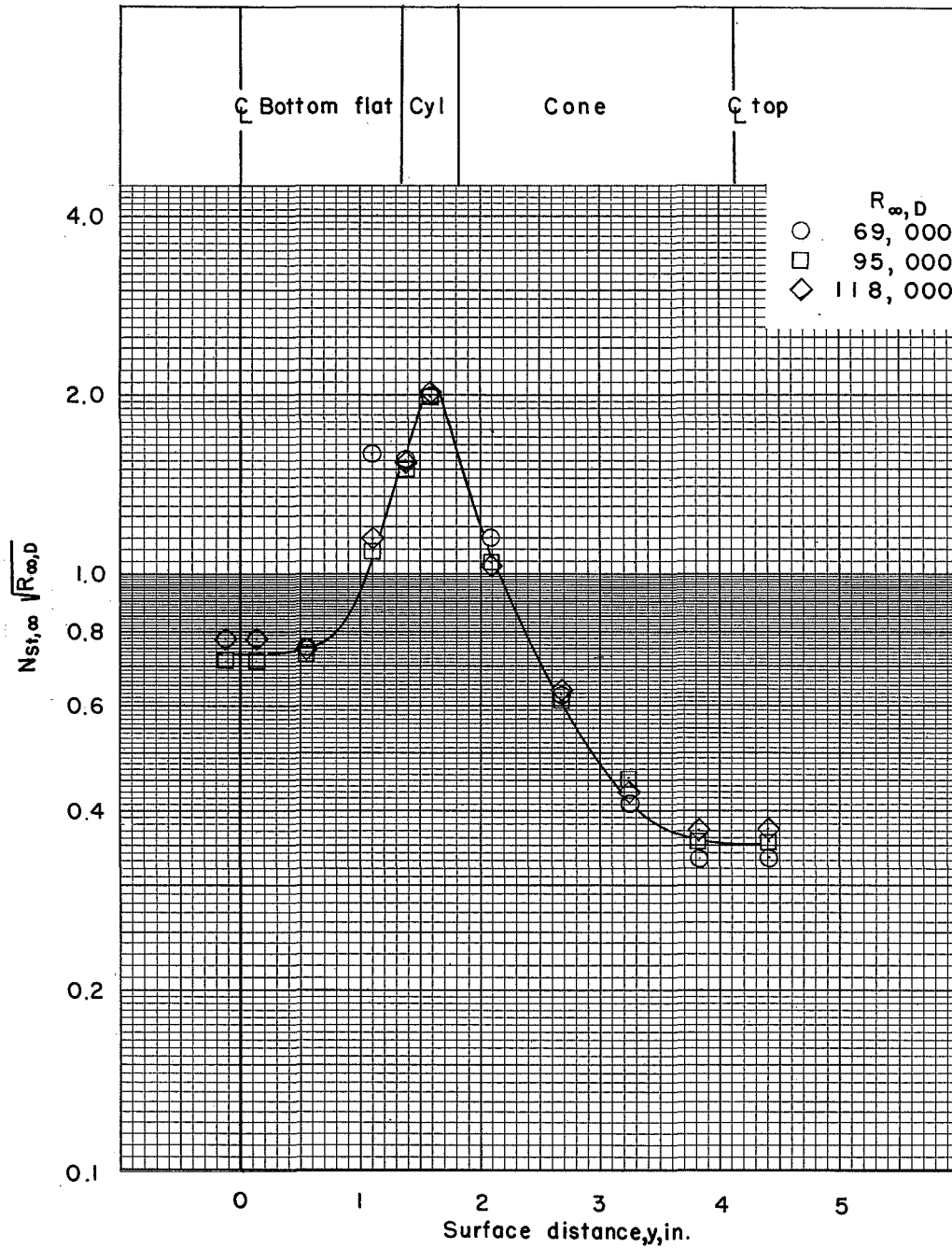
Figure 11.- Concluded.



(a) Station 1.25.

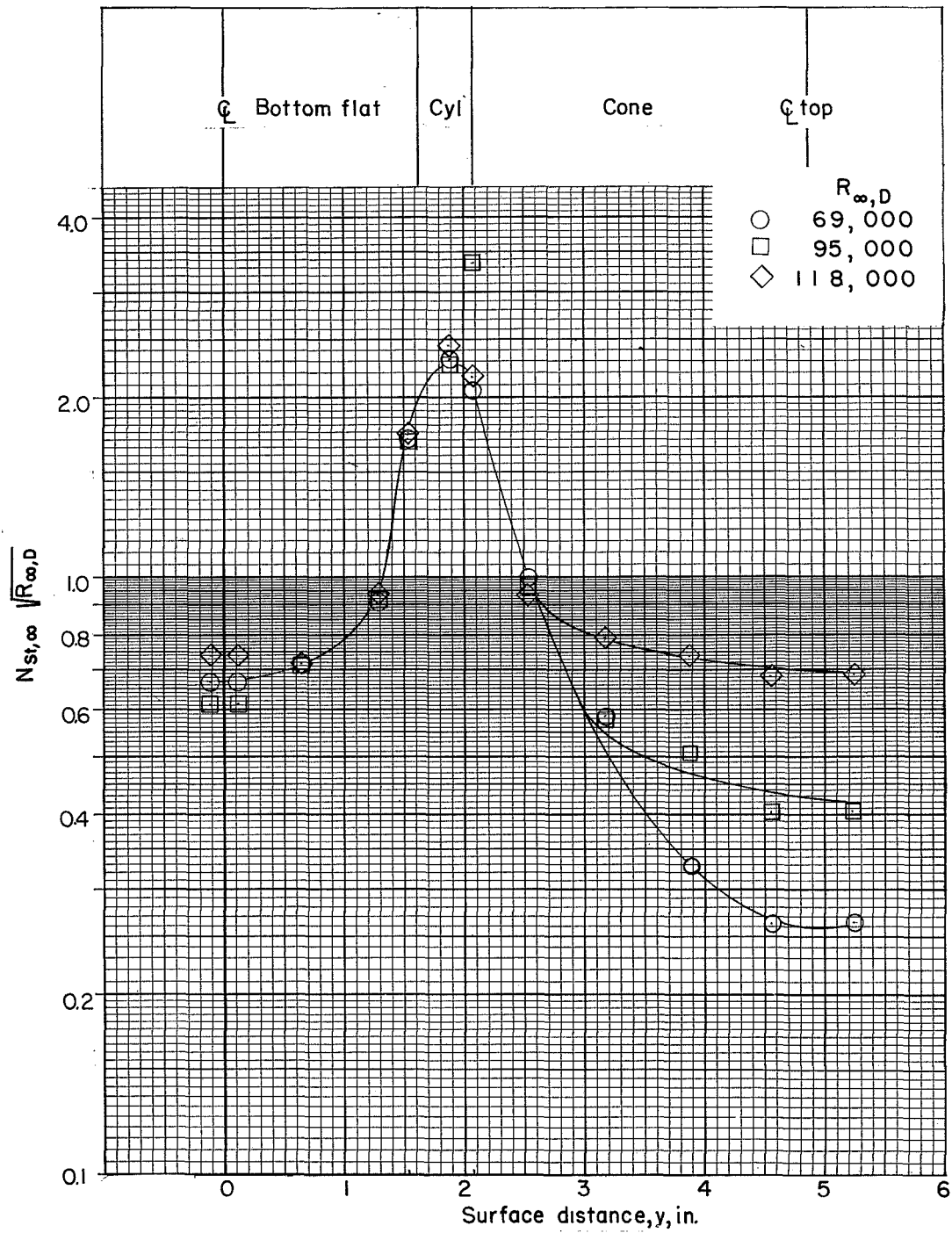
Figure 12.- Effect of Reynolds number on circumferential heat-transfer distribution at $\alpha = 15^\circ$.

L-1602



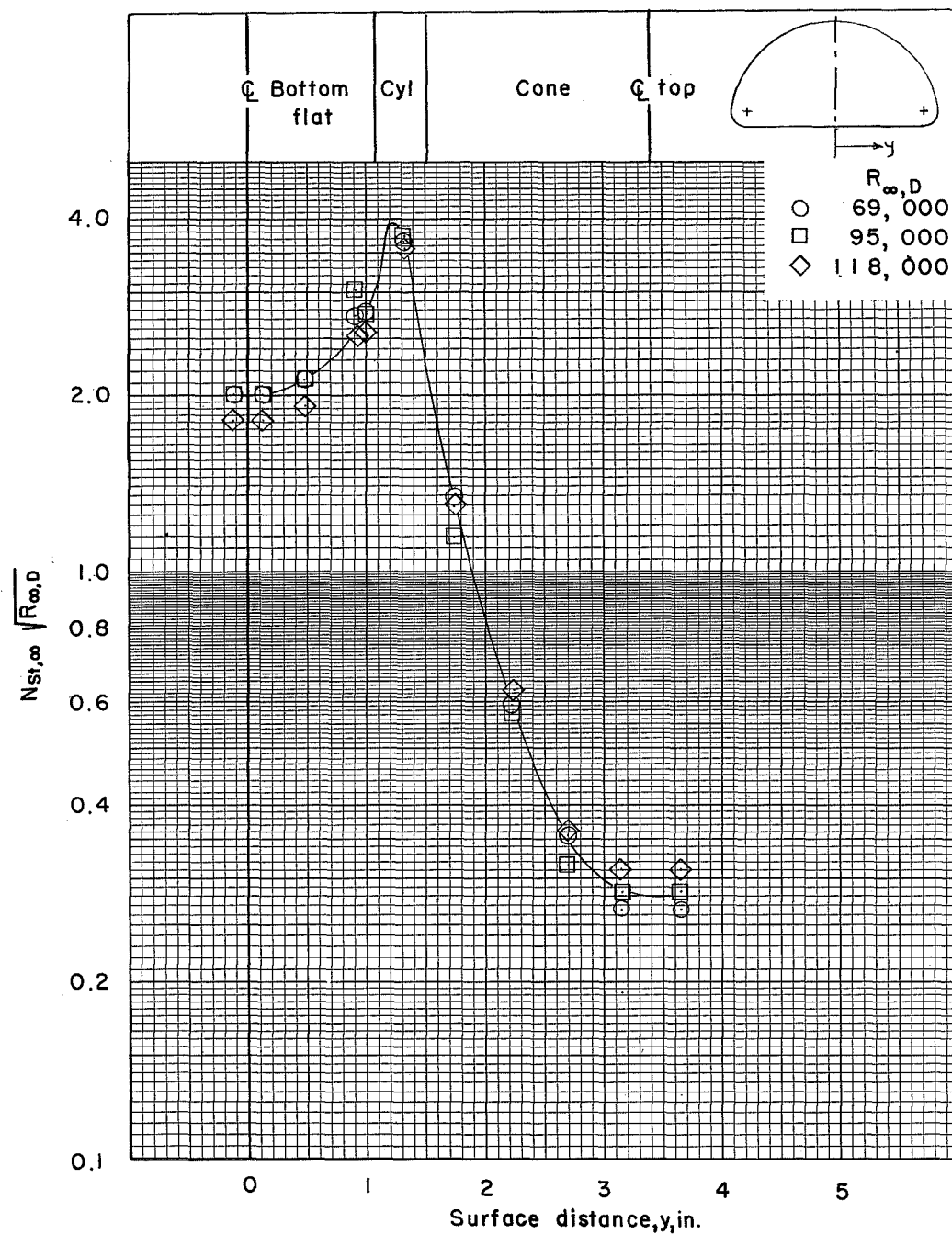
(b) Station 2.00.

Figure 12.- Continued.



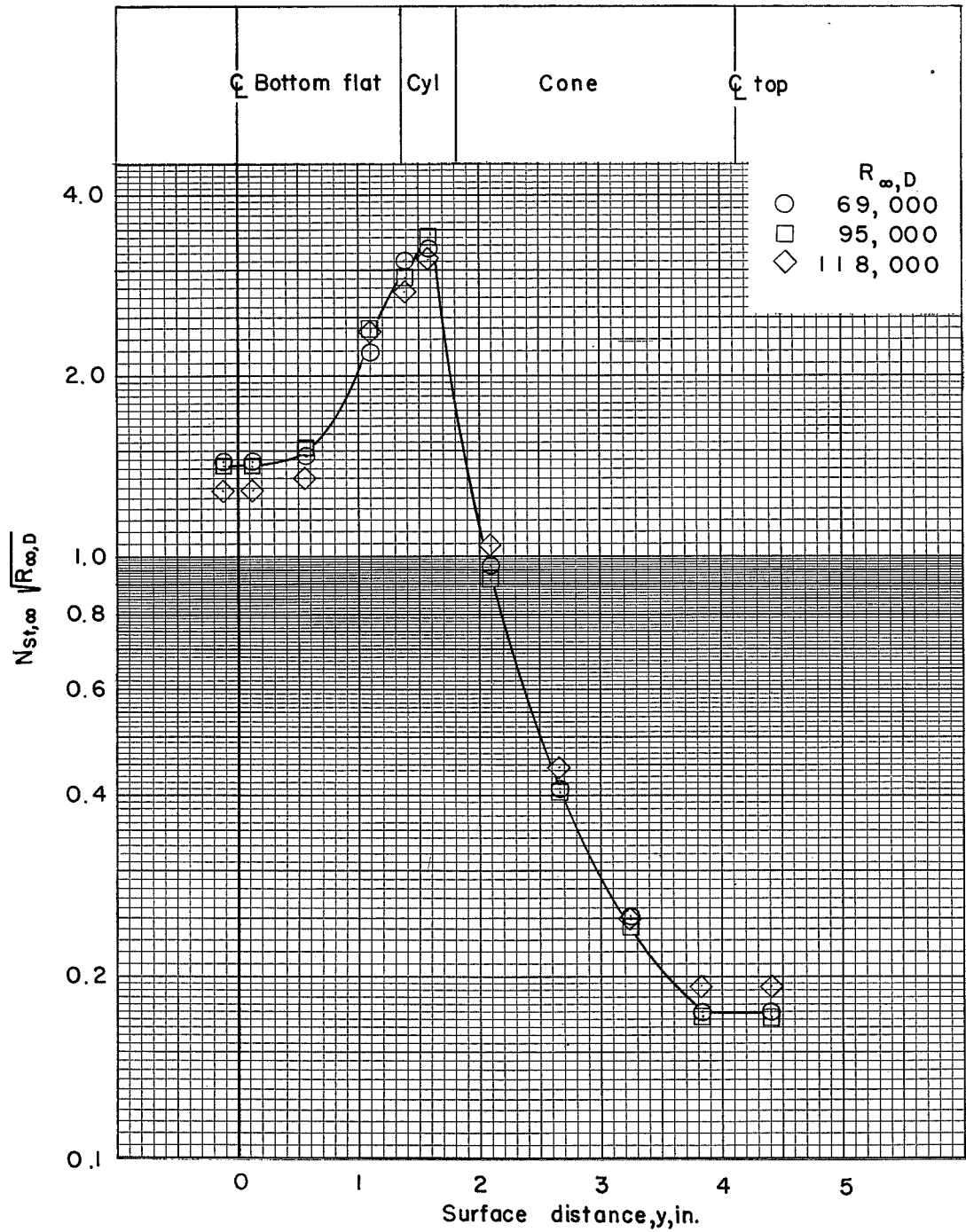
(c) Station 2.75.

Figure 12.- Concluded.



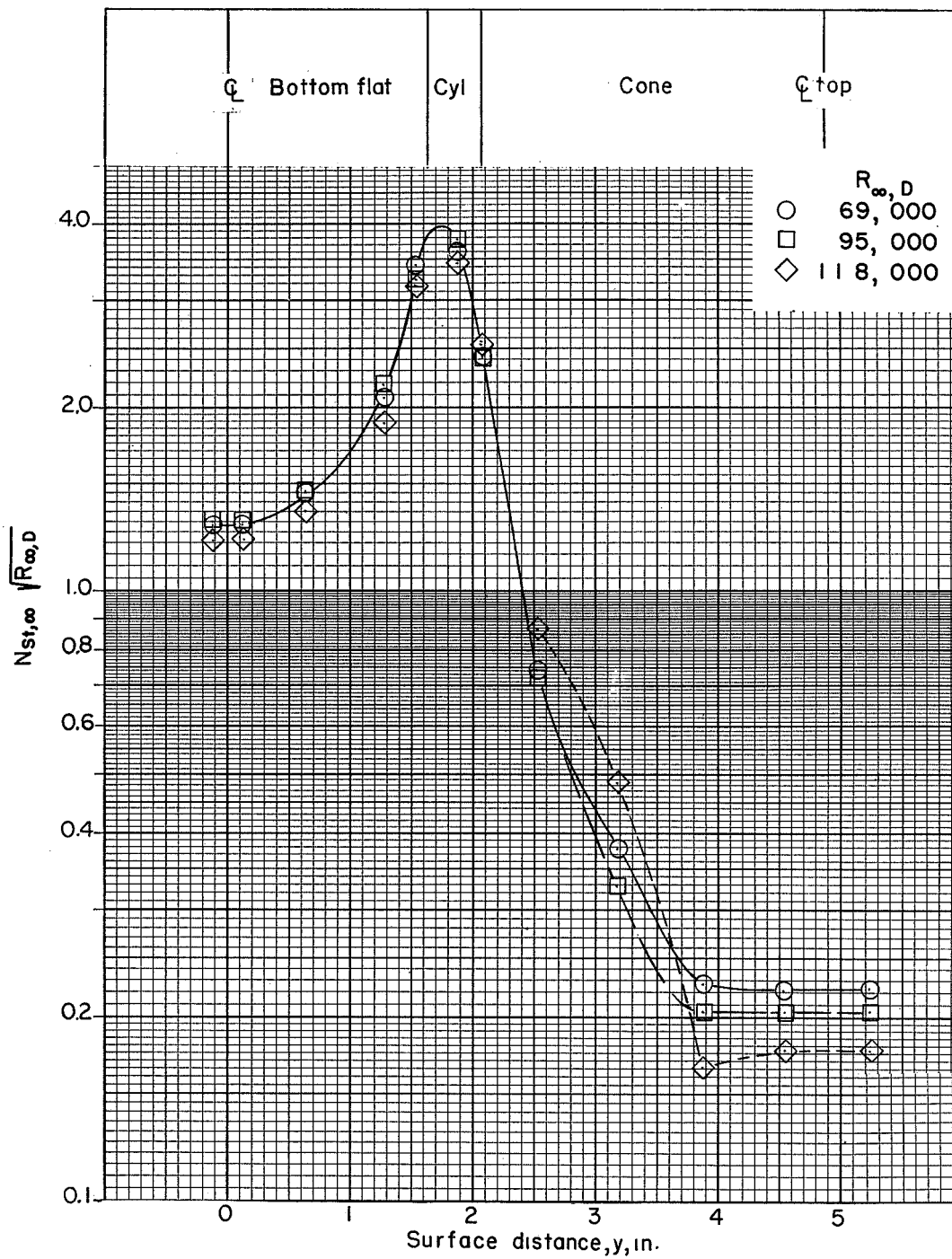
(a) Station 1.25.

Figure 13.- Effect of Reynolds number on circumferential heat-transfer distribution at $\alpha = 30^\circ$.



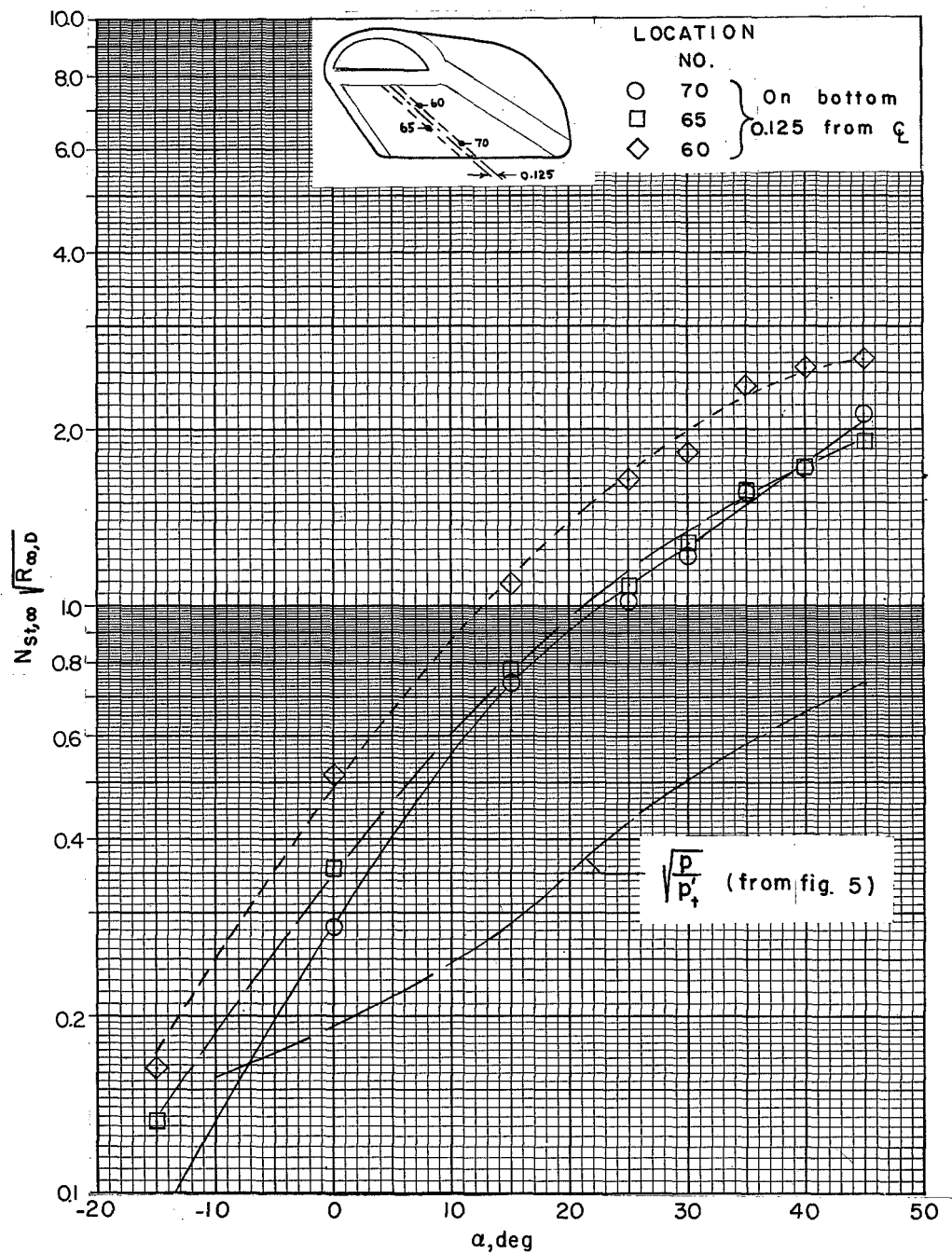
(b) Station 2.00.

Figure 13.- Continued.



(c) Station 2.75.

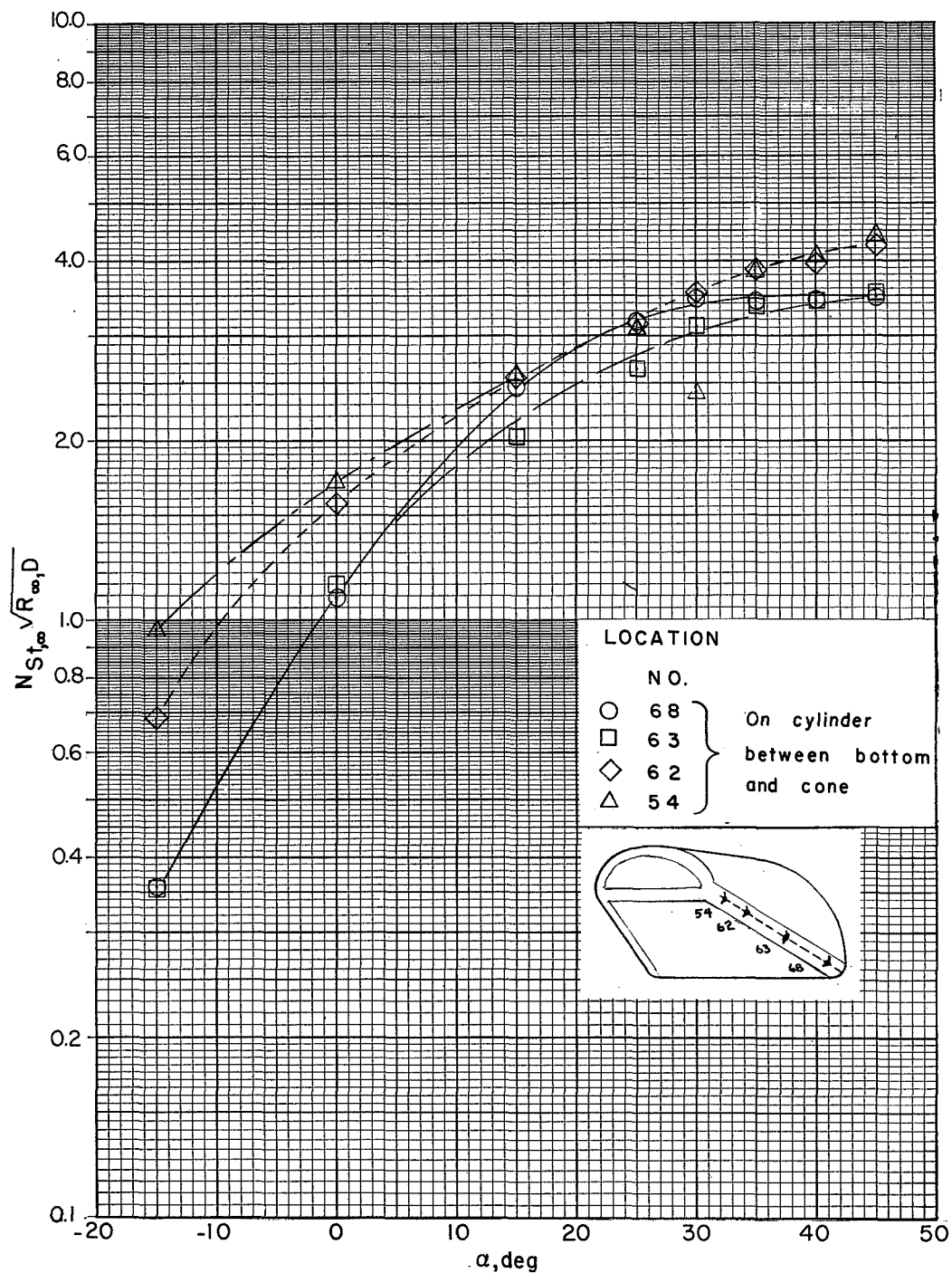
Figure 13.- Concluded.



(a) Along center line of bottom.

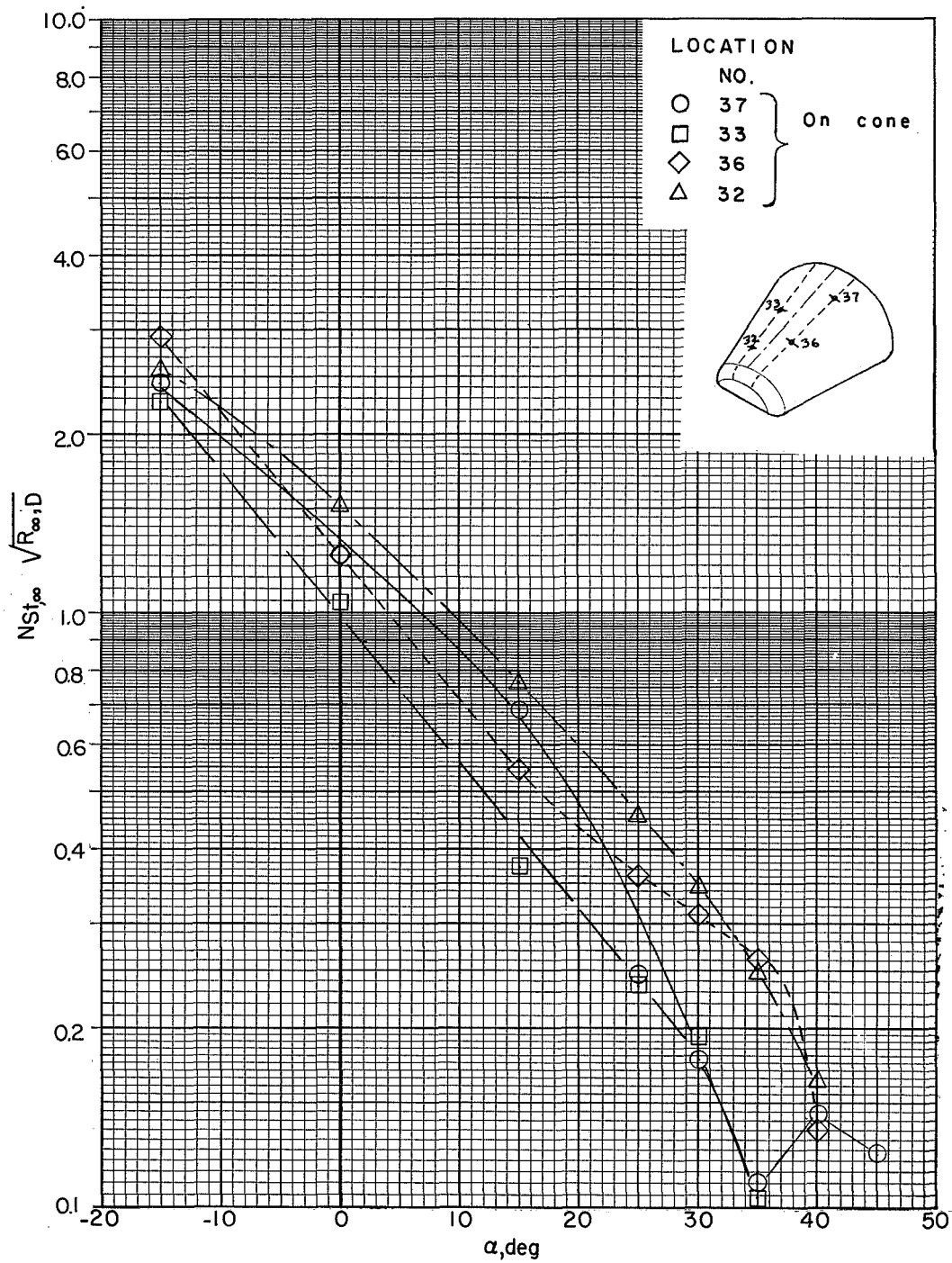
Figure 14.- Variation of heat transfer with angle of attack at selected stations.

L-1602



(b) Along cylindrical edge.

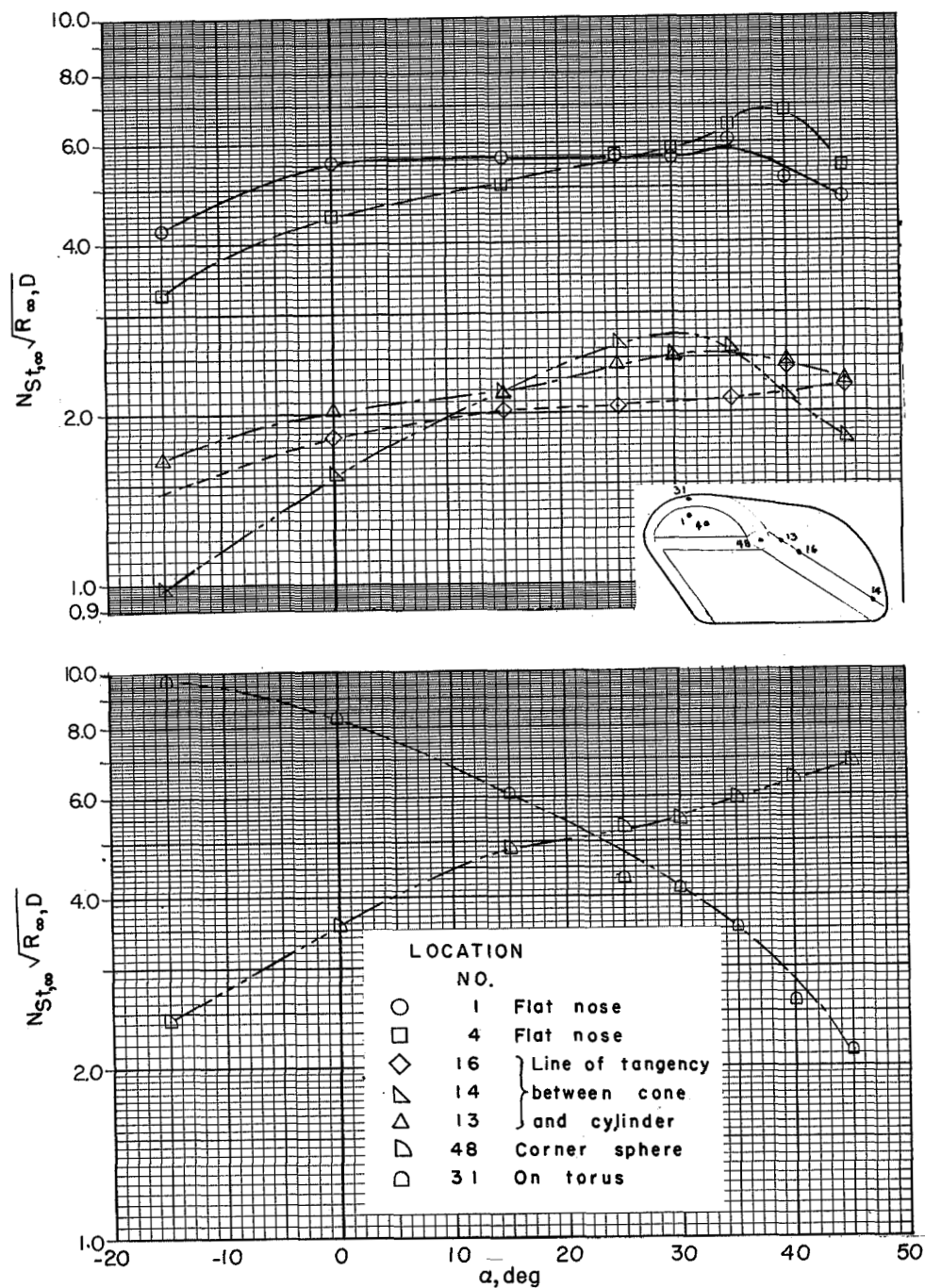
Figure 14.- Continued.



(c) Along center line of top.

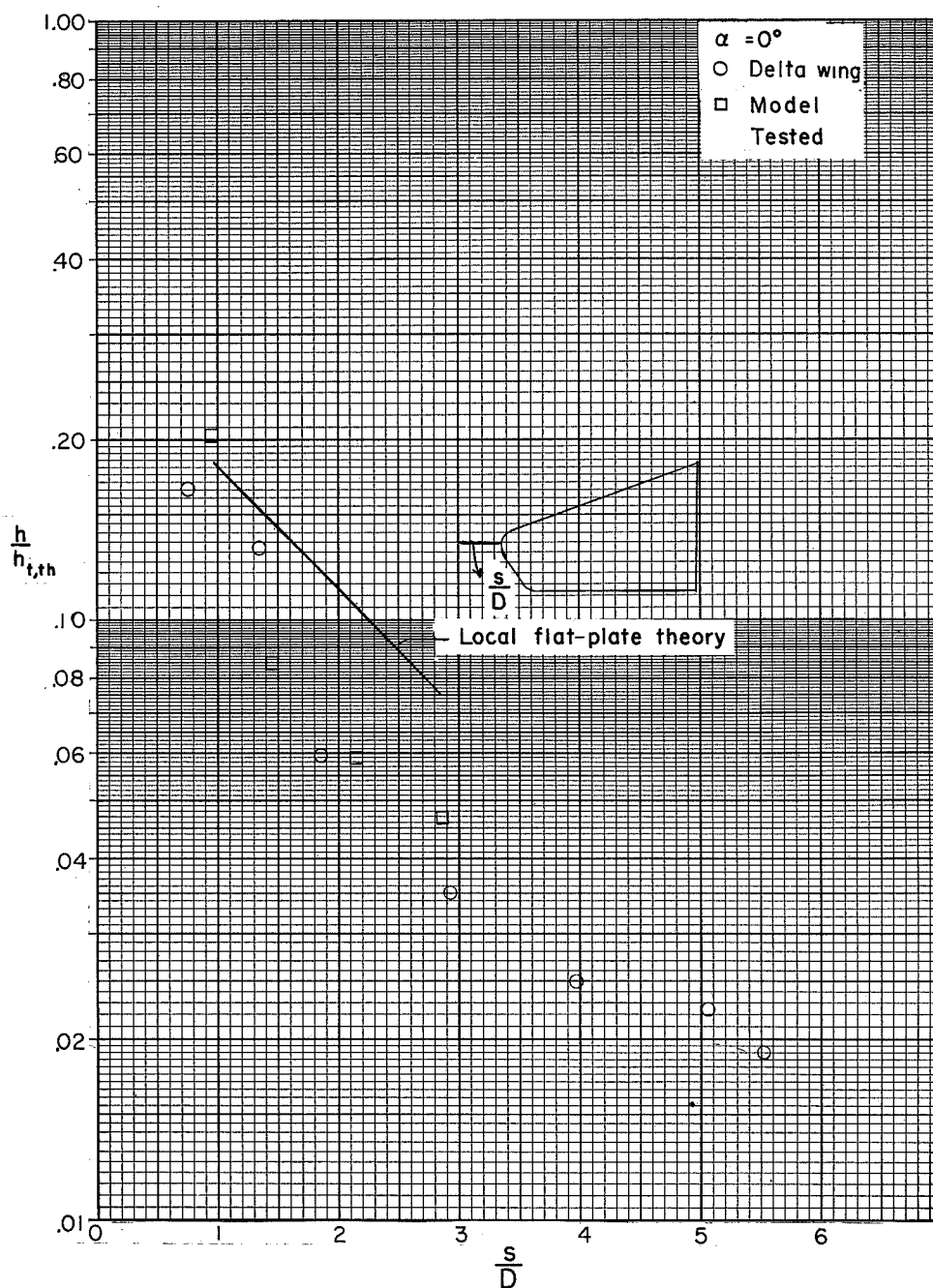
Figure 14.- Continued.

L-1602



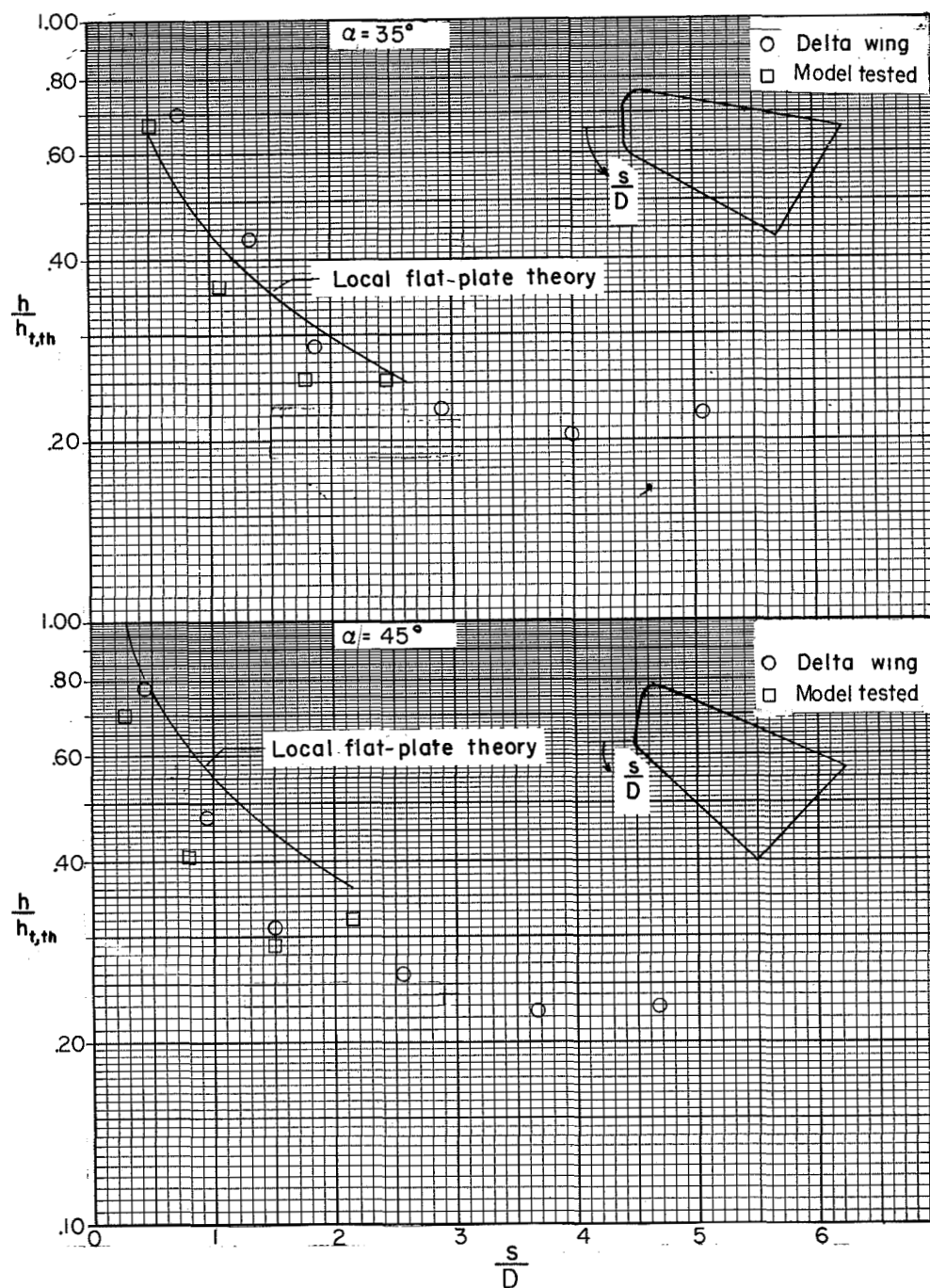
(d) Miscellaneous.

Figure 14.- Concluded.



(a) $\alpha = 0^\circ$.

Figure 15.- Comparison of heat transfer obtained along center line of bottom with results obtained from delta-wing tests and with theory.



(b) $\alpha = 35^\circ$ and 45° .

Figure 15.- Concluded.

